Acta Pharmaceutica Sinica B 2026;16(3):1550−1567

Chinese Pharmaceutical Association
Institute of Materia Medica, Chinese Academy of Medical Sciences

Acta Pharmaceutica Sinica B

www.elsevier.com/locate/apsb
www.sciencedirect.com

ORIGINAL ARTICLE

Flavescensines A−L: Novel azaspiro[4.4] heterodimeric alkaloids from *Sophora flavescens* protect against liver injury by inhibiting DUSP2-mediated mitochondrial apoptosis

Xin Lian, Jianshuang Jiang, Yanan Yang, Ziming Feng, Xu Zhang, Xiang Yuan*, Peicheng Zhang*

State Key Laboratory of Bioactive Substances and Functions of Natural Medicines, Institute of Materia Medica, Chinese Academy of Medical Sciences and Peking Union Medical College, Beijing 100050, China

Received 20 May 2025; received in revised form 21 August 2025; accepted 4 November 2025

KEY WORDS

Sophora flavescens;
Leguminosae;
Azaspiro[4.4] heterodimeric alkaloids;
Flavescensine J;
Liver injury;
DUSP2;
Mitochondrial apoptosis;
PI3K/Akt/JNK pathway

Abstract By employing a targeted strategy integrating a building blocks-based molecular network (BBMN), network annotation propagation (NAP), ultraviolet spectroscopy (UV), and mass spectrometry (MS), twelve novel spirocyclic heterodimeric alkaloid flavescensines A−L (**1**−**12**) with 5/6/6/6/5 and 6/5/6/6/5 pentacyclic skeletons were isolated from *Sophora flavescens*. Their structures were unambiguously elucidated through comprehensive spectroscopic data, quantum chemical calculations, and single-crystal X-ray diffraction. Structurally, these compounds represent the first examples of azaspiro[4.4] alkaloids formed through the inert ring A or B of the C_{15} matrine-type alkaloid and C_9 units. Notably, the NMR signals of C-9′ methylene can serve as diagnostic indicators to determine the absolute configuration of the spiro carbon. A plausible biosynthetic pathway involving an unusual pattern of [3 + 2] cycloaddition was proposed. The hepatoprotective activities of **1**−**12** were evaluated *in vitro*, and **10** exhibited the most significant activity. Further *in vivo* experiments demonstrated that **10** dramatically inhibited the APAP-induced increase in the serum ALT, AST, and LDH levels, reversed the depletion of hepatic GSH, and attenuated hepatic centrilobular necrosis and hemorrhage. Mechanistically, **10** exhibits a potential interaction with DUSP2 and inhibits its expression, thereby suppressing DUSP2-mediated mitochondrial apoptosis *via* PI3K/Akt/JNK pathway. This represents the first discovery of DUSP2 involving in the hepatoprotection.

*Corresponding authors.
E-mail addresses: yuanxiang@imm.ac.cn (Xiang Yuan), pczhang@imm.ac.cn (Peicheng Zhang).

Peer review under the responsibility of Chinese Pharmaceutical Association and Institute of Materia Medica, Chinese Academy of Medical Sciences.

https://doi.org/10.1016/j.apsb.2025.12.019

1. Introduction

Liver injury is a common type of liver disease induced by viruses or overdose of drugs and alcohol[1]. As liver injury progresses, the liver exhibits varying degrees of inflammation, necrosis, and liver fibrosis[2]. Matrine-type alkaloids, a class of bis-quinolizidine alkaloids with a 6/6/6/6 tetracyclic skeleton, display antiviral[3], antibacterial[4], and anti-inflammatory activities[5]. In recent studies, their novel dimers have been reported to demonstrate protective effects on virus- or drug-induced liver injury. For example, dimeric alkaloids flavesines A−F from *Sophora flavescens* and alopecuroides A−E from *S. alopecuroides*, which were connected *via* C−C or C−N single bonds, exhibited antiviral activities against the hepatitis B virus[6]. Additionally, sophoralines A−C, [2 + 2] cycloaddition dimers from *S. alopecuroides*, showed hepatic protective abilities in APAP-induced liver injury[7]. Moreover, matrine-indolizine and epimeric normatrine−julolidine heterodimers[8] isolated from *S. alopecuroides* significantly restricted HBsAg secretion and ameliorated virus-induced liver injury. Therefore, diverse matrine-based alkaloids may hold substantial potential as medications for liver diseases and have captured our considerable interest.

S. flavescens Ait. (known as "Ku Shen" in China) is a perennial herbaceous plant belonging to the family Leguminosae that is used as a traditional Chinese medicine for the treatment of dysentery, pruritus, trichomoniasis vaginitis, and skin suppurative infection. Previous phytochemical and pharmacological studies have revealed that alkaloids, flavonoids, dibenzoyl derivatives, triterpenoids, and phenolic acids were isolated from *S. flavescens*, and that these compounds exhibited antitumor, anti-inflammatory, antimicrobial, and antiallergic activities[9]. Among these compounds, matrine-type alkaloids, such as matrine, oxymatrine, and sophocarpine, have been reported to be the main bioactive ingredients[10]. To date, 55 matrine-type alkaloids have been reported[4,6,11-16], including 6 dimeric alkaloids that inhibited virus-induced liver injury[6].

To explore the diverse matrine-based alkaloids with hepatoprotective activities from *S. flavescens*, a targeted strategy integrating a building blocks-based molecular network (BBMN)[17,18], network annotation propagation (NAP)[19], ultraviolet spectroscopy (UV), and mass spectrometry (MS) was conducted. Surprisingly, twelve novel azaspiro[4.4] heterodimeric alkaloids (**1**−**12**) with 5/6/6/6/5 and 6/5/6/6/5 pentacyclic skeletons were isolated (Fig. 1). Their structures were elucidated *via* spectroscopic methods, quantum chemical calculations of NMR and ECD, and single-crystal X-ray diffraction. Structurally, these compounds represent the first examples of spirocyclic heterodimeric alkaloids formed through the inert ring A or B of matrine-type alkaloid and C_9 phenylpropanoid units. A plausible biosynthetic pathway was proposed. Compounds **1**−**12** were investigated for their hepatoprotective abilities in APAP-induced HepG2 cells, and **10** exhibited the most significant activity *in vitro*. Furthermore, **10** markedly ameliorated APAP-induced hepatic centrilobular necrosis and hemorrhaging, reversed the increase in the serum ALT, AST, and LDH levels, and prevented the rapid

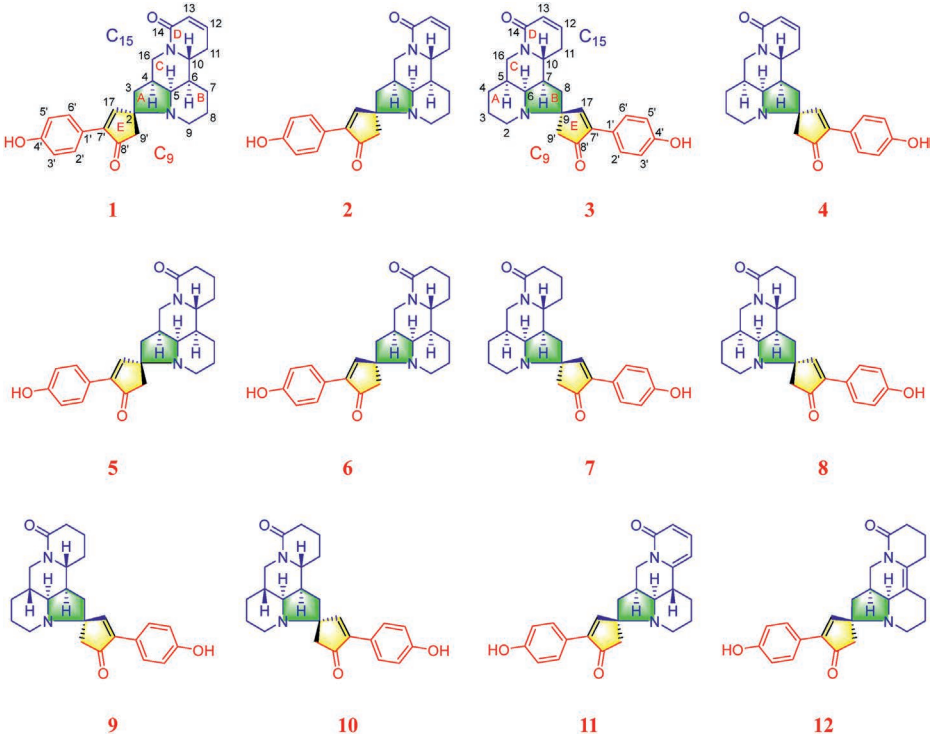

Figure 1 Chemical structures of compounds **1**−**12**.

consumption of hepatocyte GSH *in vivo*. Pharmacological mechanism revealed that **10** protected against APAP-induced acute liver injury by inhibiting the DUSP2-mediated mitochondrial apoptosis *via* PI3K/Akt/JNK pathway.

2. Results

2.1. Targeted isolation of spirocyclic heterodimeric alkaloids

The air-dried powdered roots of *S. flavescens* were percolated and decocted with 1% aqueous AcOH to obtain a crude extract, which was subjected to an HP-20 macroporous resin column and eluted with a gradient of EtOH/H_2O to provide fractions A−F. To isolate the dimeric alkaloids specifically, the isolation process started with a preliminary evaluation of these fractions, focusing on their chemical composition by using a BBMN strategy. A feature-based molecular network[20-24] with annotated nodes for known compounds was first constructed with the assistance of the MZmine software and GNPS website. For homodimers or heterodimers of matrine-based alkaloids, the product ions at *m/z* 148.11 (corresponding to the quinolizidine core arising from L-lysine) and *m/z* 249.19 or 247.18 (corresponding to the representative matrine-type alkaloids such as matrine or sophocarpine) were subsequently used as diagnostic ions to generate a BBMN of these compounds[25]. Through the analysis of the BBMN, fraction E was determined to be rich in matrine-based alkaloid dimers and was selected as the isolated fraction. However, to precisely identify special alkaloids, networks of organic nitrogen compounds were further screened by NAP. The characteristic network cluster was selected according to its distinctive precursor ions of *m/z* 391.20 and 393.22, which differ from those of known matrine-type alkaloid dimers. To recognize these target compounds, molecular networks, UV, and MS were integrated, and twelve spirocyclic heterodimeric alkaloids (**1**−**12**) were isolated (Fig. 2 and Supporting Information Figs. S1−S3).

2.2. Structural elucidation of compounds *1*−*12*

Compound **1** was obtained as a yellowish-white amorphous powder. The HRESIMS peak at *m/z* 391.2010 $[M + H]^+$ (calcd. for $C_{24}H_{27}N_2O_3$, 391.2016) indicated a molecular formula of $C_{24}H_{26}N_2O_3$ and thirteen degrees of unsaturation. The IR spectrum revealed the presence of an α,β-unsaturated amide group (1660 cm^{-1}) and a benzene ring (1595, 1512, and 1436 cm^{-1}). The ^1H NMR spectrum (Supporting Information Table S1) revealed two olefinic protons at δ_H 6.36 (1H, m) and 6.09 (1H, ddd, J = 9.5, 2.5, 1.5 Hz), two methylenes connected to heteroatoms at δ_H 4.54 (1H, dd, J = 12.5, 6.0 Hz), 2.73 (1H, t, J = 12.5 Hz), 2.60 (1H, dt, J = 11.0, 3.5 Hz), 2.10 (1H, td, J = 11.0, 3.5 Hz), and a methine at δ_H 3.83 (1H, m). These data were similar to the characteristic signals of sophocarpine. Additionally, two pairs of aromatic protons at δ_H 8.11 (2H, d, J = 8.5 Hz) and 7.32 (2H, d, J = 8.5 Hz) from a *para*-substituted benzene ring were present in the ^1H NMR spectrum. The ^{13}C NMR (Table S1) and HSQC spectra showed a total of 24 carbons for two carbonyl carbons (δ_C 205.9 and 164.7), ten olefinic carbons (δ_C 160.2, 159.6, 141.9, 138.5, 130.1, 130.1, 125.1, 123.4, 116.8, and 116.8), one quaternary carbon (δ_C 66.7), four methines including two connected to heteroatoms (δ_C 62.5, 52.2, 37.9, and 36.5), and seven methylenes, including two connected to heteroatoms (δ_C 51.0, 46.3, 45.7, 40.3, 25.9, 25.8, and 22.0). Except for the signals of the C_{15} alkaloid unit, the remaining nine carbon resonances indicated the existence of a C_9 unit. The carbonyls, double bonds, and a benzene ring accounted for eight of the thirteen degrees of unsaturation, which suggested that **1** has a pentacyclic ring system.

The ^1H−^1H COSY spectrum of **1** revealed the presence of a spin system (C-3 to C-9/C-13/C-16) similar to that of sophocarpine (Fig. 3A). The HMBC correlations from H-5/H_2-7 to C-10, H_2-9 to C-5/C-7, H-10 to C-14, H-12 to C-10/C-14, and H_2-16 to C-5/C-10/C-14 suggested the existence of a B/C/D ring system similar to that of sophocarpine. The HMBC correlations from H-4/H-5 to C-2, H_2-16 to C-3, and H-17 to C-3 indicated that the six-membered ring A of the C_{15} unit was rearranged into a five-membered ring. Additionally, the HMBC cross peaks from H-2′/H-6′ to C-4′/C-7′, H-3′/H-5′ to C-1′, and H_2-9′ to C-7′/C-8′ confirmed the presence of a C_9 phenylpropanoid unit. The correlations from H_2-9′ to C-7′/C-8′ and H-17 to C-9′ in the HMBC spectrum implied that an α,β-conjugated cyclopentenone was

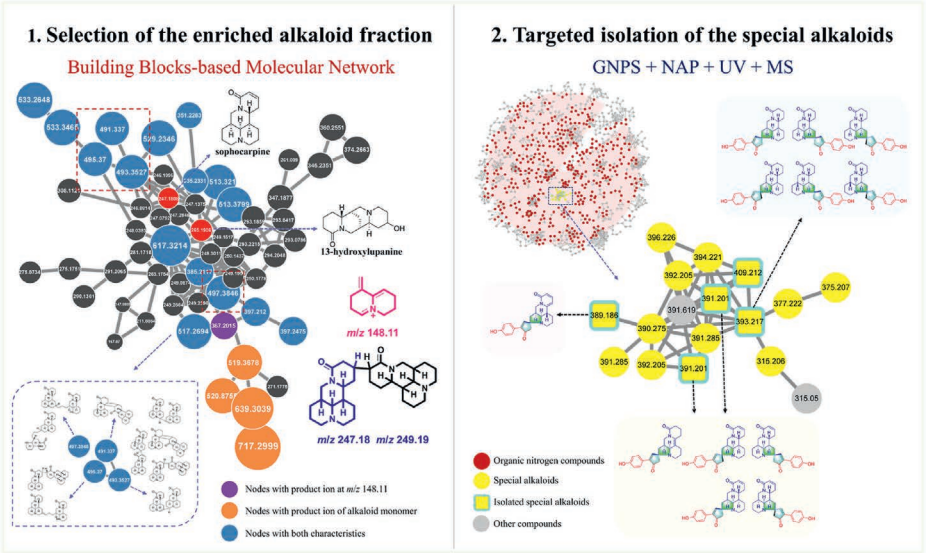

Figure 2 A workflow for targeted isolation of spirocyclic heterodimeric alkaloids.

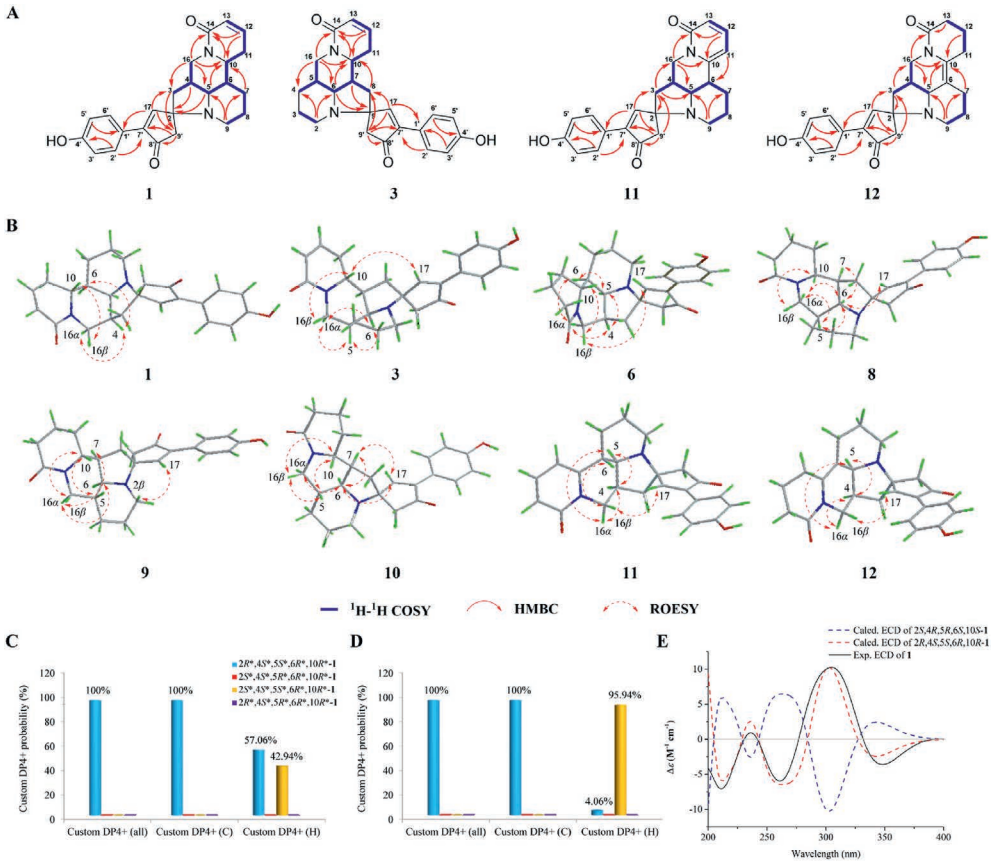

Figure 3 Structural elucidation of azaspiro[4.4] heterodimeric alkaloids. (A) Key ^{1}H−^{1}H COSY and HMBC correlations of compounds **1**, **3**, **11**, and **12**. (B) ROESY correlations of compounds **1**, **3**, **6**, **8**, and **9**−**12**. (C, D) Custom DP4+ analysis of the experimental *versus* calculated NMR chemical shifts of four possible isomers of **1** calculated at the mPW1PW91/6-31+g(d,p) and B3LYP/6-31+g(d,p) levels, respectively. (E) Experimental ECD curve of **1** and calculated ECD curves of enantiomers calculated at the CAM-B3LYP/6-31+g(d,p) level.

present in **1**. An azaspiro[4.4] ring was formed between the C_{15} and C_9 units, which was supported by the correlations from H_2-3 to C-9′ and H-17 to C-1′. Consequently, compound **1** was characterized as a heterodimeric alkaloid with a 5/6/6/6/5 pentacyclic skeleton.

The relative stereochemistry of **1** was partially deduced from the ROESY data. The correlations of H-4/H-6, H-4/H-16α, and H-10/H-16β in the ROESY spectrum suggested that H-4 and H-6 had the same spatial orientation, whereas H-10 was assigned to the opposite side (Fig. 3B). The relative configurations of C-2 and C-5 were not determined because of the overlapping H-5. Therefore, ^{1}H and ^{13}C NMR chemical shift calculations of four possible isomers of **1** were performed. Based on the R^2 coefficients of the ^{13}C NMR chemical shifts and custom DP4+ probability of 100%, the isomer with 2*R**,4*S**,5*S**,6*R**,10*R** configuration was in closer accordance with the experimental data of **1** (Fig. 3C and D). Furthermore, the absolute configurations of **1** were confirmed by comparing the experimental ECD curve with the calculated curves at the CAM-B3LYP/6-31+g(d,p) level in methanol with the PCM model. The experimental curve matched well with the calculated curve of (2*R*,4*S*,5*S*,6*R*,10*R*)-**1** in the range of 200 to 400 nm (Fig. 3E). A single crystal of **1** suitable for X-ray diffraction (Cu Kα) was obtained *via* slow volatilization from MeOH. Consistent with the structure deduced above, its absolute configurations 2*R*,4*S*,5*S*,6*R*,10*R* [Flack parameter of 0.3(5)] (Fig. 4) were confirmed, and the stereochemistry of 4*S*,5*S*,6*R*,10*R* was concordant with that of sophocarpine. Therefore, the structure of **1** was identified as depicted in Fig. 1, and it was named flavescensine A.

Compound **2** exhibited the same molecular formula as **1** ($C_{24}H_{26}N_2O_3$) based on its HRESIMS ion peak at *m/z* 391.2015 [M + H]$^+$ (calcd for $C_{24}H_{27}N_2O_3$, 391.2016). Analysis of the 1D and 2D NMR data (Supporting Information Table S1 and Fig. S4A) suggested that **2** had the same planar structure as that of **1**. Further analysis of the ROESY data showed correlations of H-4/H-16α, H-5/H-6, H-5/H-16α, and H-10/H-16β, indicating that the relative configurations of C-4, C-5, C-6, and C-10 in the C_{15} unit were identical to those of **1** (Fig. S4B). Obviously, **1** and **2** were a pair of epimers at C-2. This deduction was supported by the ROESY correlation of H-16β/H-17. Careful comparison of the ^{13}C NMR data (Table S1) of **1** and **2** revealed that the chemical shift of C-9′ shifted from δ_C 51.0 in **1** to δ_C 42.9 in **2**. Ultimately, the absolute configuration of **2** was unambiguously confirmed as 2*S*,4*S*,5*S*,6*R*,10*R* by single-crystal X-ray diffraction with a Flack parameter of [−0.03(16)] (Fig. 4), and **2** was named flavescensine B.

Compound **3** was isolated as a yellowish-white amorphous powder with the same molecular formula as **1** ($C_{24}H_{26}N_2O_3$) according to the HRESIMS ion peak at *m/z* 391.2011 [M + H]$^+$ (calcd for $C_{24}H_{27}N_2O_3$, 391.2016). Detailed analysis of the NMR data (Supporting Information Table S3) indicated that **3** was also composed of C_{15} and C_9 units. Interpretation of the HMBC correlations from H-2′/H-6′ to C-4′/C-7′, H-3′/H-5′ to C-1′, H-17 to

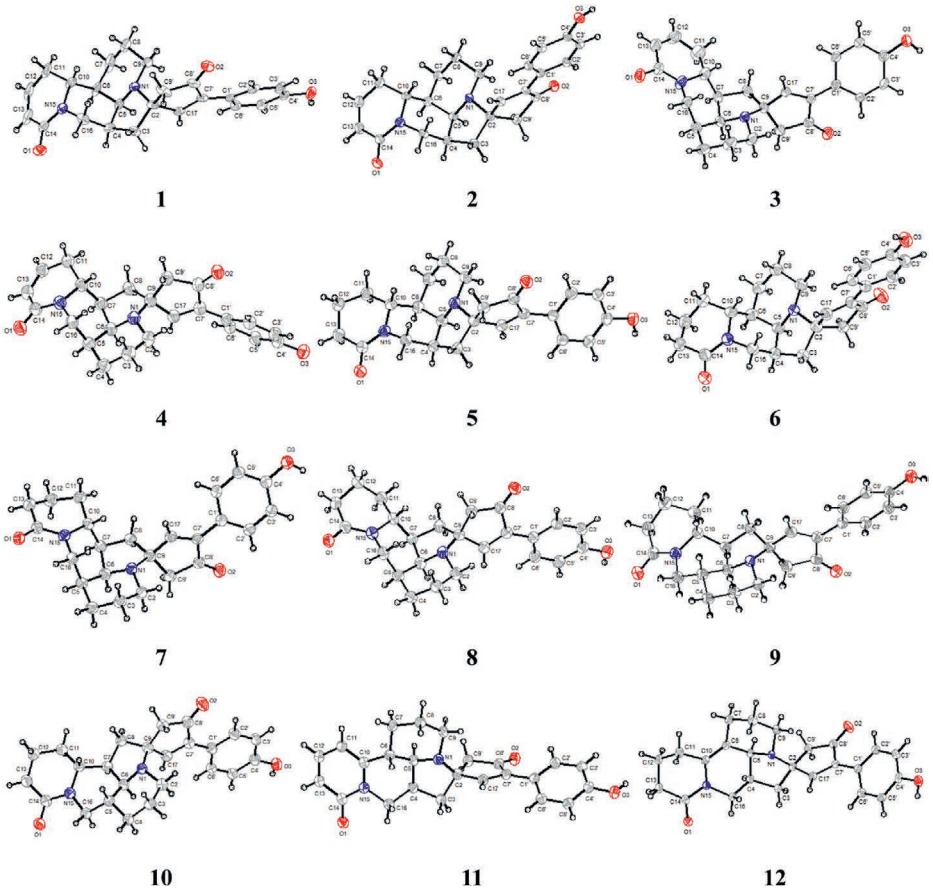

Figure 4 X-ray ORTEP drawings of **1**−**12**.

C-9′, and H_2-9′ to C-7′/C-8′ suggested that the C_9 unit of **3** was identical to that of **1** (Fig. 3A) and that an *α,β*-conjugated cyclopentanone fragment existed. However, the HMBC correlations from H-17 to C-8, H_2-9′ to C-8, H-6/H-7 to C-9, and H_2-8 to C-10 revealed that the azaspiro[4.4] ring was constructed on ring B in **3**, instead of ring A in **1**.

The ROESY correlations of H-5/H-6, H-5/H-16*α*, H-6/H-16*α*, H-10/H-16*β*, and H-10/H-17 suggested that H-5 and H-6 were cofacial, and that H-10 and H-17 were attributed to the opposite side (Fig. 3B). The relative configuration of C-7 was assigned by NMR calculations, and 5*S**,6*S**,7*R**,9*R**,10*R**-**3** was in closer accordance with the experimental data of **3** based on the R^2 coefficients of the ^{13}C NMR chemical shifts and custom DP4+ probability of 100% (Supporting Information Fig. S8). Finally, **3** was clarified by single-crystal X-ray diffraction as 5*S*,6*S*,7*R*,9*R*,10*R* with a Flack parameter of [−0.08(15)] (Fig. 4) and named flavescensine C.

Compound **4** exhibited the same molecular formula as **3** ($C_{24}H_{26}N_2O_3$) according to its HRESIMS ion peak at *m/z* 391.2010 $[M + H]^+$ (calcd for $C_{24}H_{27}N_2O_3$, 391.2016). The 1D and 2D NMR data (Table S3 and Fig. S4A) suggested that **4** possessed the same planar structure as **3**, and the correlations of H-5/H-6, H-5/H-16*α*, H-6/H-17, and H-10/H-16*β* in the ROESY spectrum indicated that the relative configurations of C-5, C-6, C-9, and C-10 were 5*S**,6*S**,9*S**,10*R** (Fig. S4B). However, assignment of the relative configuration of C-7 was hampered because of the overlapping protons. The results of the NMR chemical shift computations revealed that 5*S**,6*S**,7*R**,9*S**,10*R**-**4** was highly consistent with that of experimental data (Supporting Information Fig. S11). Obviously, **4** was an epimer at C-9 of **3**. Detailed comparison of their ^{13}C NMR data (Table S3) revealed that the chemical shift of C-9′ shifted from δ_C 43.1 in **3** to δ_C 51.0 in **4**. Furthermore, Cu K*α* X-ray crystallographic analysis with a Flack parameter [0.07(10)] assigned the absolute configuration of **4** as 5*S*,6*S*,7*R*,9*S*,10*R* (Fig. 4), which was named flavescensine D.

Compounds **5** and **6** were obtained as yellowish-white amorphous powders and gave the same molecular formula of $C_{24}H_{28}N_2O_3$ from the HRESIMS ion peak at *m/z* 393.2163 $[M + H]^+$ (calcd. for $C_{24}H_{29}N_2O_3$, 393.2173), requiring twelve degrees of unsaturation. Compared with the NMR data of **1** (Supporting Information Tables S1 and S2), the absence of olefinic signals indicated that the C_{15} unit in **5** and **6** was similar to matrine. Furthermore, the correlations of H-4/H-5, H-4/H-16*α*, H-5/H-6, and H-10/H-16*β* in the ROESY spectrum revealed that their relative configurations of C-4, C-5, C-6, and C-10 were 4*S**,5*S**,6*R**,10*R**. The ROESY correlations of H-5/H-17 in **5** and H-16*β*/H-17 in **6** suggested that the relative configuration was 2*R** in **5** and 2*S** in **6** (Fig. 3B and Fig. S4B). Compounds **5** and **6** were a pair of epimers at C-2, and the chemical shift of C-9′ shifted from δ_C 51.1 in **5** to δ_C 43.6 in **6**. In addition, the absolute configurations of **5** and **6** were unambiguously substantiated as 2*R*,4*S*,5*S*,6*R*,10*R* and 2*S*,4*S*,5*S*,6*R*,10*R* with Flack parameters of [0.08(13)] and [−0.1(2)], respectively (Fig. 4). Thus, the structures of **5** and **6** were established as shown in Fig. 1, and they were named flavescensines E and F, respectively.

Compounds **7** and **8** were ascertained to have the molecular formula $C_{24}H_{28}N_2O_3$, as deduced from the HRESIMS ion peak at *m/z* 393.2162 $[M + H]^+$ (calcd for $C_{24}H_{29}N_2O_3$, 393.2173). The HMBC correlations from H_2-2 to C-6, H-6/H-7 to C-9, H-10 to C-14, H_2-16 to C-4/C-10/C-14, H-17 to C-8/C-1′/C-9′, H-2′/H-6′ to C-4′/C-7′, H-3′/H-5′ to C-1′, and H_2-9′ to C-7′/C-8′ indicated that the planar structures of **7** and **8** were highly similar to that of **3**, except that the double bond between C-12 and C-13 was saturated (Fig. S4A)**.** The ROESY cross peaks of H-5/H-6, H-6/H-7, H-5/H-16α, H-6/H-16α, H-6/H-17, and H-10/H-16β in **8** suggested that the relative configurations were 5*S**,6*S**,7*R**,9*S**,10*R** (Fig. 3B). Owing to the overlapping protons at the chiral centers in the ^{1}H NMR spectrum of **7**, the relative configurations of C-5, C-6, C-7, C-9, and C-10 were determined *via* NMR computations and partial ROESY correlations. The custom DP4+ probability of 100% of diastereomer 5*S**,6*S**,7*R**,9*R**,10*R**-**7** matched well with the experimental data (Supporting Information Fig. S14). This was supported by the ROESY correlations of H-10/H-16β and H-10/H-17 (Fig. S4B). X-ray analysis of single crystals revealed their absolute configurations as 5*S*,6*S*,7*R*,9*R*,10*R* in **7** and 5*S*,6*S*,7*R*,9*S*,10*R* in **8**, with Flack parameters of [−0.21(14)] and [0.11(11)] (Fig. 4), which were named flavescensines G and H, respectively.

Compounds **9** and **10** were isolated as yellowish-white amorphous powders and possessed the same planar structures as **7** ($C_{24}H_{28}N_2O_3$) based on their HRESIMS and 2D NMR data (Fig. S4A). A careful comparison of their ^{13}C NMR data with the corresponding data of **7** (Supporting Information Tables S3 and S4) revealed a large change in the signals of C-3/C-4/C-5/C-6/C-16. The ROESY correlations of H-5/H-10, H-5/H-16β, H-6/H-7, H-6/H-16α, and H-10/H-16β revealed that H-6, H-7, and H-10 had the same spatial orientation as **7**, whereas H-5 changed from α-oriented in **7** to β-oriented in **9** and **10**. Similarly, **9** and **10** were a pair of epimers at C-9, which was supported by the ROESY correlations of H-2β/H-17 in **9** and H-6/H-7/H-17 in **10** (Fig. 3B). Ultimately, the absolute configurations of **9** and **10** were assigned as 5*R*,6*S*,7*R*,9*R*,10*R* and 5*R*,6*S*,7*R*,9*S*,10*R* by single-crystal X-ray diffraction analysis *via* Cu Kα radiation with Flack parameters of [0.31(15)] and [0.11(12)] (Fig. 4), and were named flavescensines I and J, respectively.

Compound **11** was obtained as a yellowish-white amorphous powder, and the HRESIMS ion peak at *m/z* 389.1857 $[M + H]^+$ (calcd for $C_{24}H_{25}N_2O_3$, 389.1860) provided a molecular formula of $C_{24}H_{24}N_2O_3$, suggesting fourteen degrees of unsaturation. Detailed analysis of the corresponding ^{1}H and ^{13}C NMR data revealed that a methylene (δ_C 26.4) and a methine (δ_C 52.3) in **2** were replaced by two olefinic carbons (δ_C 101.1 and δ_C 150.3) in **11** (Tables S1 and S2). The HMBC correlations from H-12/H_2-16 to C-10 and H-11 to C-6 implied that an extra olefinic bond was present at C-10 in **11** (Fig. 3A). Furthermore, the ROESY correlations of H-4/H-5, H-4/H-16α, H-5/H-16α, H-6/H-16β, and H-16β/H-17 indicated that H-4 and H-5 had the same orientation, and H-6 and H-17 were assigned to the opposite side (Fig. 3B). Single-crystal X-ray diffraction analysis unambiguously confirmed the absolute configuration of **11** as 2*S*,4*S*,5*S*,6*R* with a Flack parameter of [0.06(5)] (Fig. 4), and this compound was named flavescensine K.

Compound **12** was obtained as a yellow amorphous powder, and the HRESIMS ion peak at *m/z* 391.2012 $[M + H]^+$ (calcd. for $C_{24}H_{27}N_2O_3$, 391.2016) represented a molecular formula of $C_{24}H_{26}N_2O_3$, indicating thirteen degrees of unsaturation. The NMR data were similar to those of **6** (Table S2), except that two methines (δ_C 53.4 and δ_C 41.0) were replaced by quaternary carbons (δ_C 129.7 and δ_C 116.2). The HMBC data from H-5/H_2-7/H_2-12/H_2-16 to C-10 further confirmed that an olefinic bond, $\Delta^{6/10}$, existed in **12** (Fig. 3A). Moreover, the ROESY correlations of H-4/H-5, H-4/H-16α, H-5/H-16α, and H-16β/H-17 implied that H-4 and H-5 had the same orientation, whereas H-17 was assigned to the opposite side (Fig. 3B). The absolute configuration of **12** were ultimately clarified as 2*S*,4*S*,5*S* with a Flack parameter of [0.01(7)] by single-crystal X-ray diffraction analysis (Fig. 4), and the compound was named flavescensine L.

2.3. Characteristic NMR signals for determining the configuration of the spiro carbon

Five pairs of epimers of spirocyclic heterodimeric alkaloids (**1**−**10**) were unambiguously elucidated by extensive spectroscopic analysis, especially single-crystal X-ray diffraction. The C_{15} units of compounds **1**−**8** possessed the same absolute configurations as sophocarpine and matrine. After the full assignment of their ^{1}H and ^{13}C NMR data in pyridine-d_5, some interesting phenomena related to the C-9′ methylene were observed. Here, two pairs of epimers **1** and **2** along with **3** and **4**, were analyzed as model compounds. When the C_9 unit was fused to ring A, the H_2-9′ methylene protons of **1** appeared at δ_H 2.84 (H-9′a) and δ_H 2.79 (H-9′b), whereas the corresponding protons of **2** resonated at δ_H 2.91 (H-9′a) and δ_H 2.19 (H-9′b) (Table S1). The difference in the chemical shifts of the H_2-9′ methylene protons was small ($\Delta\delta_{H\text{-}9'}$: 0.05) in **1** and large ($\Delta\delta_{H\text{-}9'}$: 0.72) in **2**. Similar results for H_2-9′ methylene were also displayed for **5** and **6**. When the C_9 unit was fused to ring B, a small value of $\Delta\delta_{H\text{-}9'}$ was observed for **4** and **8**, whereas a large value of $\Delta\delta_{H\text{-}9'}$ appeared for **3** and **7**. Based on the aforementioned data, a pattern was summarized that when $\Delta\delta_{H\text{-}9'} < 0.06$, the configuration of C-9′ was β-oriented (compounds **1**, **4**, **5**, and **8**), and the absolute configurations of the spiro carbon were *R* (C_9 unit connected to ring A) and *S* (C_9 unit connected to ring B), respectively; when $\Delta\delta_{H\text{-}9'} > 0.40$, the configuration of C-9′ was α-oriented (compounds **2**, **3**, **6**, and **7**), and the absolute configurations of the spiro carbon were *S* (C_9 unit connected to ring A) and *R* (C_9 unit connected to ring B), respectively. For **9** and **10** with 5*R*, a similar pattern to that of **7** and **8** was observed in the ^{1}H NMR spectra. **10** with 9*S* had a small value of $\Delta\delta_{H\text{-}9'}$ (0.05), and **9** with 9*R* had a large value of $\Delta\delta_{H\text{-}9'}$ (0.45) (Fig. 5).

Similarly, the characteristic signals of C-9′ of the C_9 unit were observed in their ^{13}C NMR spectra. The chemical shift of C-9′ in **1**, **4**, **5**, and **8** appeared at nearly δ_C 51.0, whereas C-9′ in **2**, **3**, **6**, and **7** resonated at approximately δ_C 43.0. When δ_C 51.0, the configuration of C-9′ was β-oriented (compounds **1**, **4**, **5**, and **8**), and the absolute configurations of the spiro carbon were *R* (C_9 unit connected to ring A) and *S* (C_9 unit connected to ring B), respectively; when δ_C 43.0, the configuration of C-9′ was α-oriented (compounds **2**, **3**, **6**, and **7**), and the absolute configurations of the spiro carbon were *S* (C_9 unit connected to ring A) and *R* (C_9 unit connected to ring B), respectively. For **9** and **10** with 5*R*, although the chemical shift of C-9′ in **9** and **10** decreased from 3 to 5 ppm, it did not affect that a small value of C-9′ ($\delta_{C\text{-}9'}$: 39.6) reflected 9*R* and a large value ($\delta_{C\text{-}9'}$: 45.8) corresponded with 9*S* (Fig. 5). Therefore, the ^{1}H and ^{13}C NMR data of the C-9′ methylene in pyridine-d_5 can be used as diagnostic signals to determine the absolute configuration of the spiro carbon.

The rational mechanisms for the patterns of $\Delta\delta_{H\text{-}9'}$ and $\delta_{C\text{-}9'}$ can be explained by their similar conformations in pyridine-d_5 and single crystal X-ray diffraction results. Compared with the ^{13}C

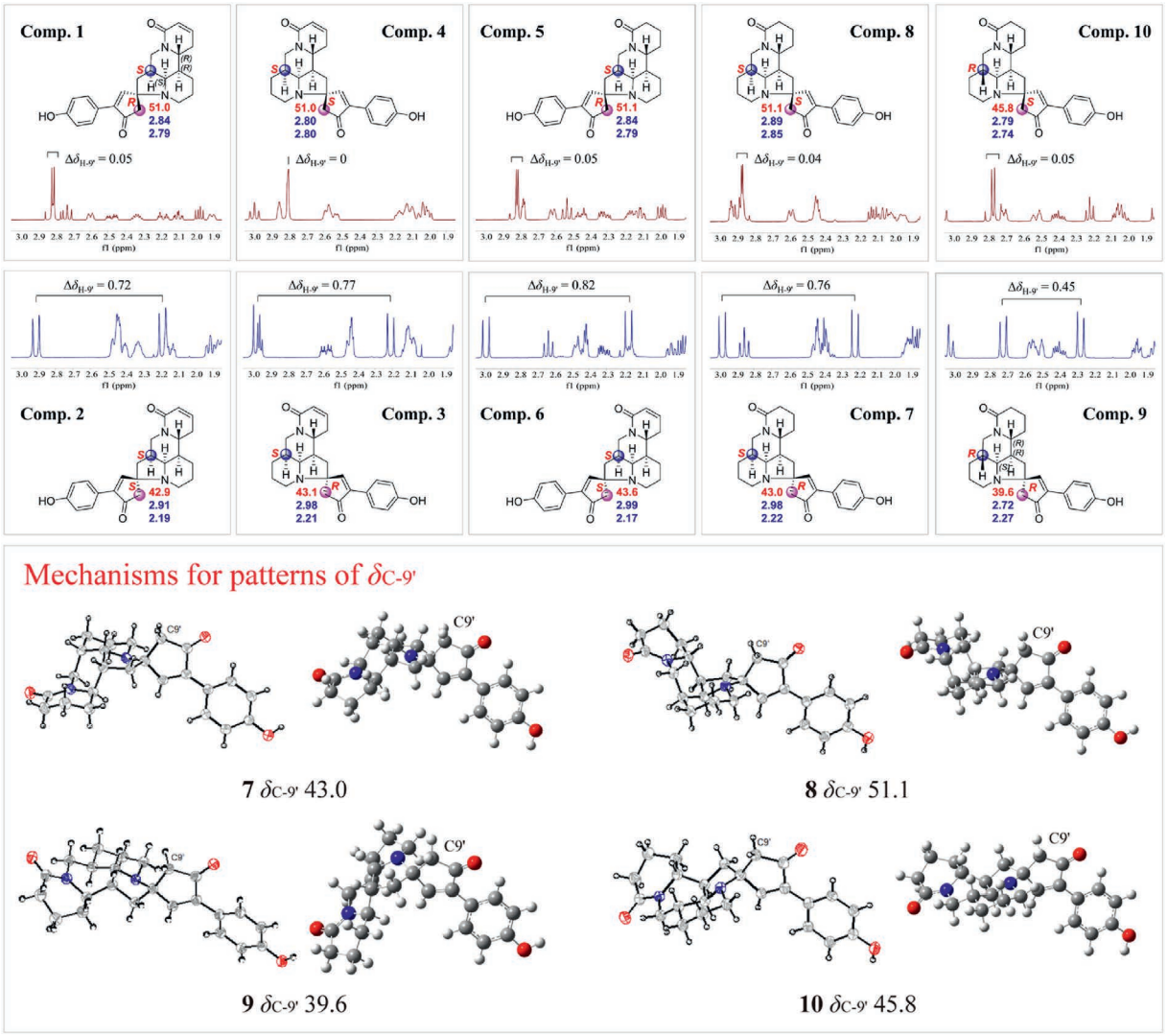

Figure 5 NMR data of C-9′ in pyridine-d_5 as diagnostic signals to determine the absolute configuration of the spiro carbon.

NMR data of C-9′ in **1**, **4**, **5**, **8**, and **10**, the small value of $\delta_{C\text{-}9'}$ in **2**, **3**, **6**, **7**, and **9** can be explained that their C_{15} units were closer to C-9′, generating γ-gauche effect. The upfield chemical shifts observed at C-9′ in **9** and **10** with 5*R* can also be attributed to a closer spatial distance between the C_{15} units and C-9′, comparing with **7** and **8** with 5*S* (Fig. 5). Moreover, the observed $\Delta\delta_{H\text{-}9'}$ deviations in the ^{1}H NMR spectra can be primarily ascribed to the chemical environment generated by the C_{15} units containing four stereocenters. Notably, due to the poor solubility in methanol, chloroform, and DMSO, the observed patterns are applicable for data acquired in pyridine-d_5. The C_{15} units should possess the same absolute configurations as sophocarpine, matrine and sophoridine. Additionally, when the C_{15} unit possessed more double bonds, the application of these patterns requires caution.

*2.4. Compound **10** attenuated APAP-induced liver injury in HepG2 cells*

The protective effects of compounds **1**−**12** against acute liver injury (ALI) were evaluated in APAP-induced HepG2 cells *in vitro*. Compounds **4**, **7**, and **9**−**11** possessed hepatoprotective potential, and **10** showed the most significant hepatoprotective activity (Fig. 6A). **10** reversed the decrease in the cell viability of APAP-induced HepG2 cells to 56.45%, compared with 51.90% in the APAP group, and exhibited hepatoprotective effects in a dose-dependent manner at concentrations of 5, 10, and 20 μmol/L (Fig. 6B and C). Therefore, **10** was chosen for subsequent experiments. The correlation between hepatic protective activity and apoptosis was further examined *via* flow cytometry. The results revealed that the percentage of apoptotic cells increased by 58.43% after exposure to APAP compared with 9.08% in the control group. Treatment with **10** significantly inhibited APAP-induced cell apoptosis, reducing the percentage of apoptotic cells to 32.57%, 30.80%, and 30.84% at concentrations of 5, 10, and 20 μmol/L, respectively, in a dose-dependent manner (Fig. 6D and E). The cell cycle distribution was subsequently analyzed. As shown in Fig. 6F and G, the results suggested that **10** relieved APAP-induced cell cycle arrest at the S phase in a dose-dependent manner. Additionally, a JC-1 staining assay was conducted to determine the mitochondrial membrane potential. Consistent with the apoptosis results, immunofluorescence analysis showed that **10** dose-dependently reduced the proportion of green fluorescence while increasing red fluorescence. MPTP staining also revealed that the opening of mitochondrial permeability transition pore was

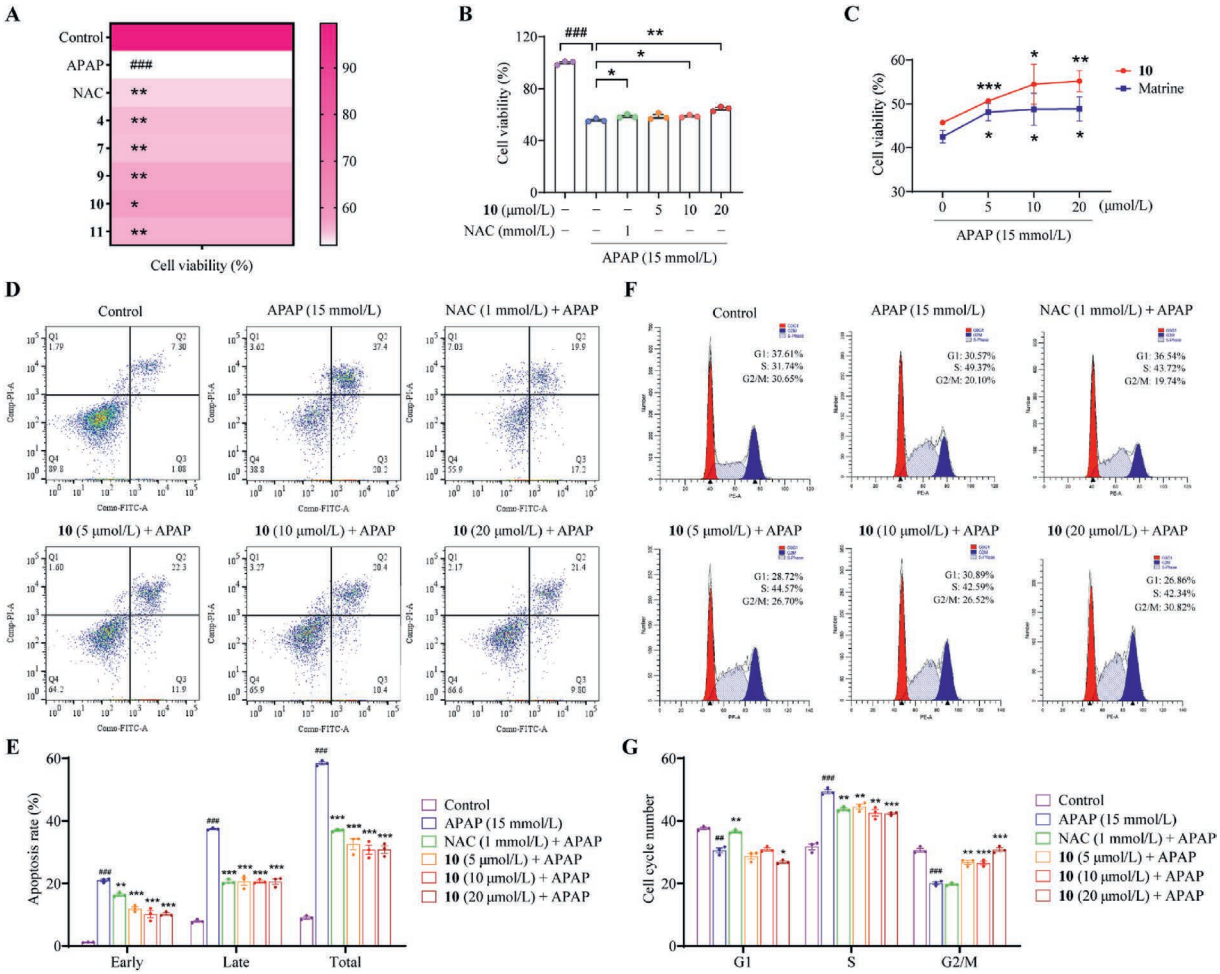

Figure 6 Hepatoprotective effect of **10** on APAP-induced liver injury *in vitro*. (A) Hepatoprotective effects of the test compounds on APAP-induced HepG2 cells. HepG2 cells were incubated with APAP (15 mmol/L) and/or the test compounds (10 μmol/L) for 24 h, and *N*-acetylcysteine (NAC) (1 mmol/L) was used as the positive control. The color of the heatmap color represents the viability of the HepG2 cells. (B, C) Hepatoprotective effects of **10** (5, 10, and 20 μmol/L) and matrine on APAP-induced HepG2 cells. (D) Hepatoprotective effect of **10** on APAP-induced apoptosis in HepG2 cells. (E) The percentage of apoptotic cells was determined by flow cytometry *via* Annexin V-FITC/PI double staining. (F) Hepatoprotective effect of **10** on the cell cycle of APAP-induced HepG2 cells. The cell cycle was analyzed by flow cytometry *via* PI staining. (G) Relative percentages of cells in the G1, S, and G2/M phases. Data are expressed as mean ± SEM, with $n = 3$ for each group; $^{\#\#}P < 0.01$, and $^{\#\#\#}P < 0.001$ compared with the control group; $^{*}P < 0.05$, $^{**}P < 0.01$, and $^{***}P < 0.001$ compared with the APAP group.

reversed in the **10**-treated groups. These findings indicate that **10** reversed the decrease in the mitochondrial membrane potential and mitochondrial permeability, which inhibited mitochondrial apoptosis in APAP-induced HepG2 cells (Fig. 7A−D). Given that **10** plays crucial roles in the regulation of mitochondrial apoptosis, immunoblotting was further performed to verify the function of this compound. The results revealed that **10** dose-dependently increased the expression of Bcl-2 and decreased the expression of Bax, cleaved caspase-3, and cleaved caspase-9 (Fig. 7E−I). In summary, these findings confirmed that **10** ameliorated APAP-induced liver injury in HepG2 cells by inhibiting mitochondria-mediated apoptosis.

*2.5. Compound **10** ameliorated APAP-induced liver injury in mice*

We next investigated whether **10** could ameliorate ALI *in vivo*. A mouse model of acute liver injury was established *via* APAP overdose[26,27]. The mice were given **10** (30 mg/kg) by intragastric administration twice at a 12 h interval. One hour after the last administration, APAP (300 mg/kg) was injected intraperitoneally. Liver tissues and plasma were collected at 3 and 6 h after APAP treatment, and the serum alanine transaminase (ALT), aspartate transaminase (AST), lactate dehydrogenase (LDH), and hepatic glutathione (GSH) levels were examined. The serum ALT, AST, and LDH levels at 3 h after APAP administration dramatically increased to 3626.00 ± 203.80, 4472.00 ± 321.21, and 12294.00 ± 856.36 U/L, respectively, and the level of hepatic GSH decreased to 0.22 ± 0.06 μmol/g, whereas it was 1.74 ± 0.08 μmol/g in the control group. Pretreatment with **10** noticeably decreased the serum ALT, AST, and LDH levels to 2294.00 ± 387.20, 1664.00 ± 342.13, and 4382.00 ± 1046.87 U/L, respectively, and prevented the depletion of hepatic GSH to 0.45 ± 0.03 μmol/g (Fig. 8A and B), relieving APAP-induced liver injury. Furthermore, 6 h after the injection of APAP, the serum ALT, AST, and LDH levels decreased in the **10**-treated

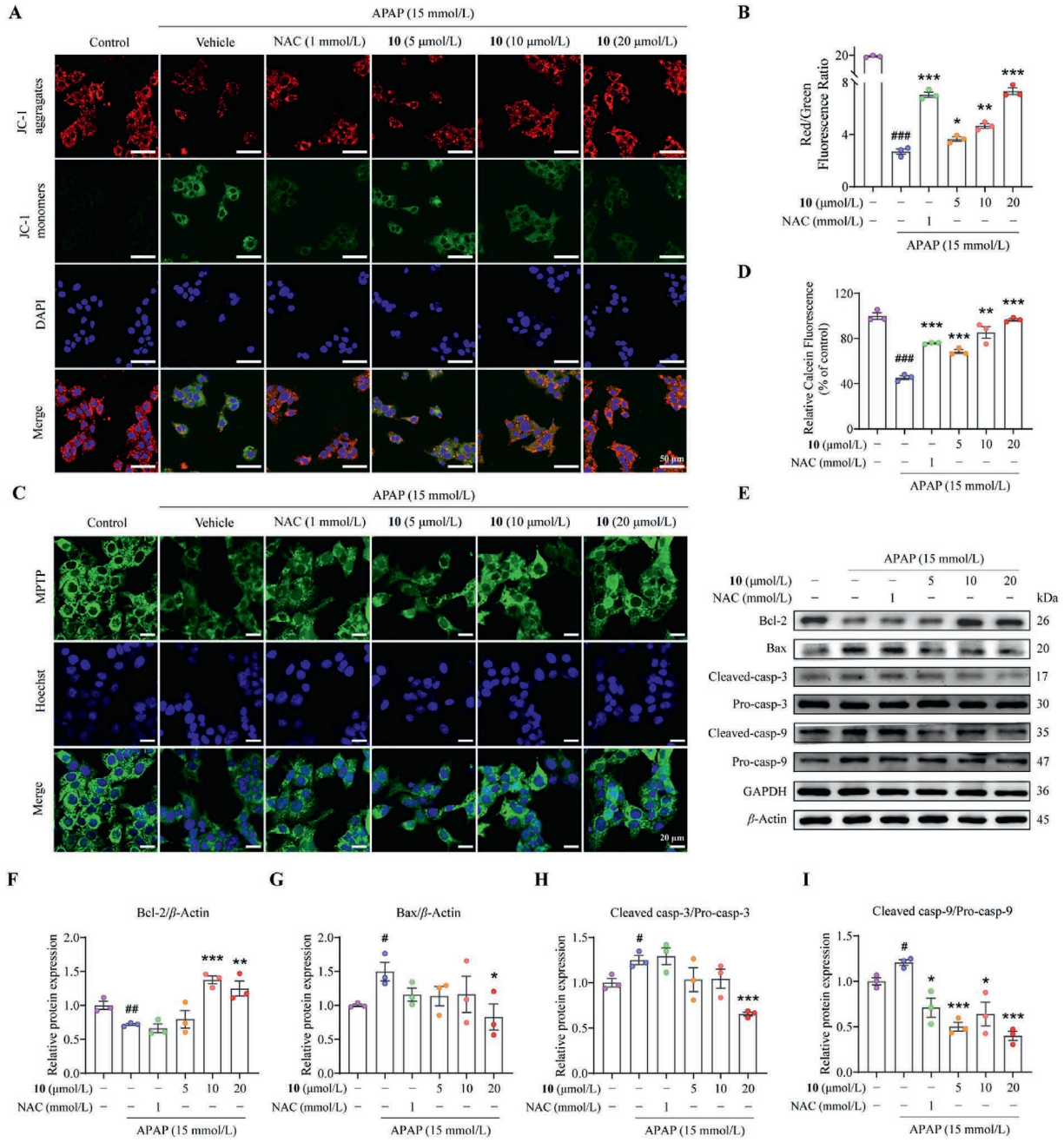

Figure 7 Inhibitory effect of **10** on mitochondria-mediated apoptosis *in vitro*. (A) Representative images of JC-1-stained HepG2 cells ($n = 3$, original magnification of 60 ×) in the control, APAP, NAC, and treated groups. Scale bar, 50 μm. (B) Quantification of the red/green fluorescence ratio determined *via* image J. (C) Representative images of Mitochondrial Permeability Transition Pore (MPTP)-stained HepG2 cells ($n = 3$, original magnification of 60 ×) in the control, APAP, NAC, and treated groups. Scale bar, 20 μm. (D) Quantification of calcein fluorescence determined *via* image J. (E−I) Western blots and quantification results of Bcl-2, Bax, cleaved caspase-3, and cleaved caspase-9 expression. β-Actin or GAPDH served as the loading control. Data are expressed as mean ± SEM of three independent experiments; $^{\#}P < 0.05$, $^{\#\#}P < 0.01$, and $^{\#\#\#}P < 0.001$ compared with the control group; $^{*}P < 0.05$, $^{**}P < 0.01$, and $^{***}P < 0.001$ compared with the APAP group.

group, whereas the rapid consumption of hepatocyte cellular GSH was reversed (Fig. 8C and D). To observe histopathological alterations in the liver, hematoxylin-eosin (H&E) staining was performed, which revealed that centrilobular necrosis was evident at 3 h after APAP administration and peaked at 6 h, accompanied by hepatomegaly and bleeding. However, these pathological injuries were alleviated in the **10**-treated group, and the liver index was also ameliorated (Fig. 8E−G). Moreover, the degree of apoptosis increased in parallel with the area of hepatic necrosis. TUNEL staining revealed that the apoptotic indices at 3 and 6 h after APAP administration significantly increased to 7.31 ± 1.07 and 29.49 ± 3.15, respectively. However, **10** decreased the apoptotic index to 2.20 ± 0.13 and 2.47 ± 0.20, respectively, revealing that **10** suppressed APAP-induced cell apoptosis *in vivo* (Fig. 8H−J). The relative expression of proteins related to mitochondria-mediated apoptosis in liver tissues was subsequently

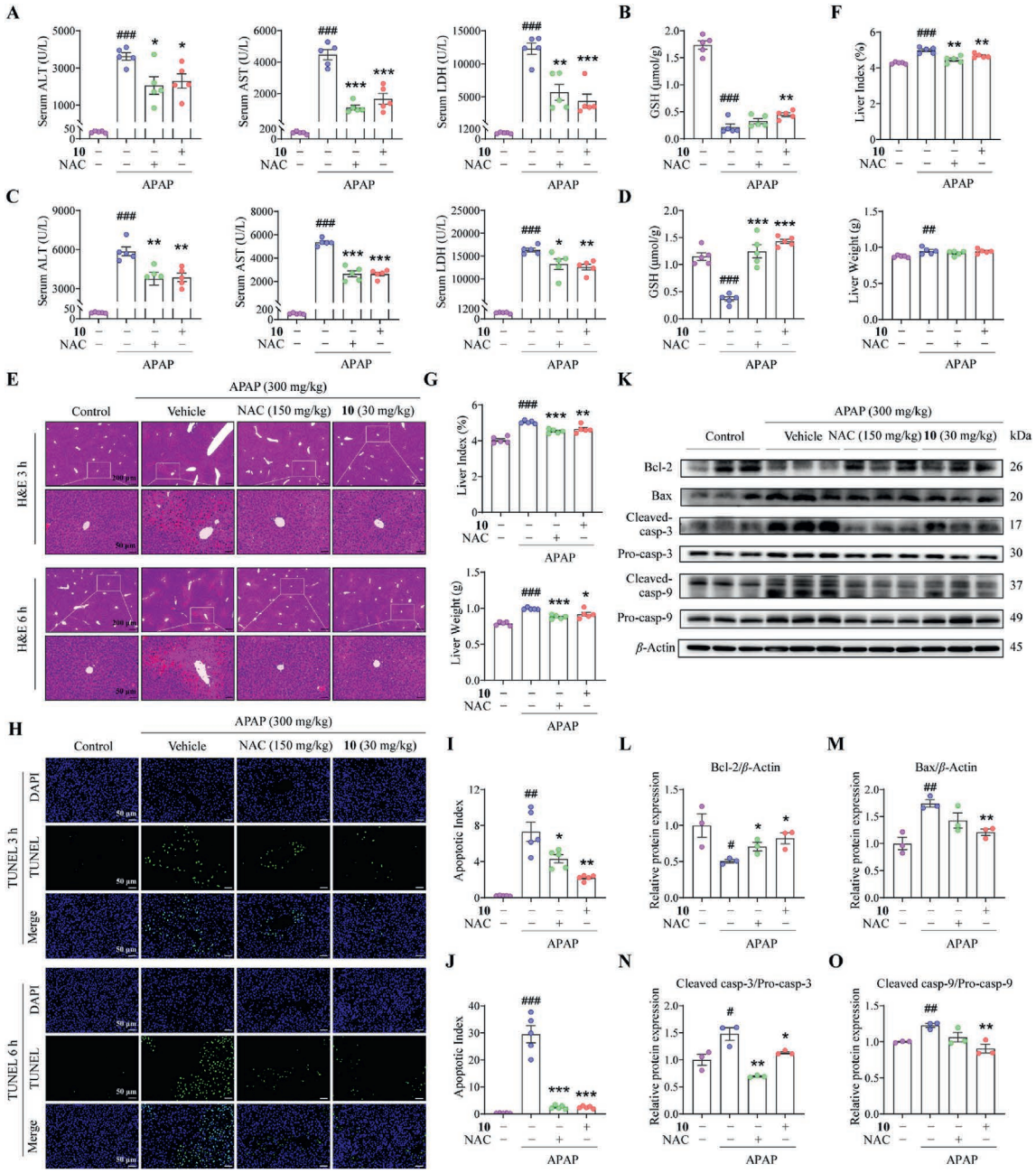

Figure 8 Hepatoprotective effect of **10** on APAP-induced liver injury and its ability to inhibit mitochondria-mediated apoptosis *in vivo*. Compound **10** and the positive control NAC were given by intragastric administration at doses of 30 and 150 mg/kg, respectively. One hour after the last gavage, APAP was administered by intraperitoneal injection at a concentration of 300 mg/kg, and 3 and 6 h later, the liver tissue and plasma were collected for further analysis ($n = 5$). (A, B) Serum ALT, AST, and LDH levels and hepatic level of GSH in APAP-induced ALI mice at 3 h after APAP administration. (C, D) Serum ALT, AST, and LDH levels and hepatic levels of GSH in APAP-induced ALI mice at 6 h after APAP administration. (E) Representative images of H&E-stained liver tissues ($n = 5$, original magnification of 5× and 20×). (F) Liver weights and liver indices of APAP-induced ALI mice at 3 h after APAP administration. (G) Liver weights and liver indices of APAP-induced ALI mice at 6 h after APAP administration. (H) Representative images of TUNEL-stained mouse liver sections ($n = 5$, original magnification of 20×) at 3 and 6 h after APAP administration. (I, J) Apoptotic indices at 3 and 6 h after APAP administration. Data are expressed as mean ± SEM, with $n = 5$ for each group; $^{\#\#}P < 0.01$, $^{\#\#\#}P < 0.001$ compared with the control group; $^{*}P < 0.05$, $^{**}P < 0.01$, and $^{***}P < 0.001$ compared with the vehicle group. (K–O) Western blots and quantification results of Bcl-2, Bax, cleaved caspase-9, and cleaved caspase-3. β-Actin served as the loading control. Data are expressed as mean ± SEM of three independent experiments; $^{\#}P < 0.05$, $^{\#\#}P < 0.01$ compared with the control group; $^{*}P < 0.05$, $^{**}P < 0.01$ compared with the APAP group.

examined *via* Western blotting. Consistent with the apoptosis results, **10** noticeably decreased the expression of Bax, cleaved caspase-3, and cleaved caspase-9, and increased the expression of Bcl-2, suggesting that **10** attenuated APAP-induced liver injury in mice by inhibiting cell apoptosis (Fig. 8K−O). Overall, these results indicate that **10** possesses excellent hepatoprotective potential *in vivo*, suggesting that **10** could serve as a hepatoprotective candidate for drug-induced liver injury.

2.6. Compound *10* alleviated mitochondrial apoptosis by inhibiting the DUSP2-mediated PI3K/Akt/JNK pathway

To further explore the hepatoprotective mechanism of **10** in APAP-induced liver injury, RNA sequencing (RNA-seq) analysis was carried out to identify differentially expressed genes (DEGs) and enriched pathways between the treated group and the APAP group. The results revealed that the expression levels of 567 genes for which $|\log_2(\text{fold change})| > 1$ and P value < 0.05 were significantly different, including 206 downregulated genes and 361 upregulated genes (Fig. 9A). A heatmap was also generated to display DEGs for which $|\log_2(\text{fold change})| > 1.5$ and P value < 0.05 (Fig. 9B); the gene *DUSP2* in particular attracted our attention owing to its downregulated expression in the treated group compared with that in the APAP group. Western blots and real time quantitative PCR analyses were conducted to verify the altered expression of DUSP2, which revealed that the relative protein and mRNA expression of DUSP2 decreased in a dose-dependent manner in the treated groups, which was in agreement with the RNA-seq results (Fig. 9C). Further KEGG analysis suggested that the DUSP2-enriched MAPK signaling pathway was involved in the hepatoprotective function of **10**. Additionally, the upstream pathway PI3K-Akt signaling pathway was enriched in KEGG pathways (Fig. 9D), and its activation signal Ras revealed enriched GO biological process gene sets, such as Ras protein signal transduction and regulation of Ras protein signal transduction (Fig. 9E). Given that the MAPK signaling pathway plays a pivotal role in the inhibitory effect of **10** on hepatocyte apoptosis, we focused on the JNK signaling pathway, which is one of the MAPK signaling pathways and responsible for regulating apoptosis[28]. Additionally, the PI3K−Akt signaling pathway among the enriched KEGG pathways could be considered as the upstream pathway of the JNK signaling pathway (Fig. 9D). To confirm the mechanism described above, the expression of proteins related to the PI3K-Akt and JNK signaling pathways in HepG2 cells and liver tissues was examined *via* Western blotting. The results showed that **10** significantly decreased the expression of p-JNK/JNK, and increased the expression of p-PI3K/PI3K and p-Akt/Akt, confirming that **10** is involved in the regulation of the PI3K/Akt/JNK signaling pathway (Fig. 9F−K).

Consistent with the Western blots *in vitro*, treatment with **10** dramatically reversed the increase in the protein and mRNA expression of DUSP2 in liver tissues (Fig. 9J, L and M), which attracted us to investigate the correlation between **10** and DUSP2. As shown in Fig. 10A, overexpression of DUSP2 inhibited the increase of cell viability in the **10**-treated group. JC-1 fluorescence analysis revealed that DUSP2 overexpression significantly reduced the proportion of red fluorescence in the APAP group. Treatment with **10** failed to restore mitochondrial membrane potential in DUSP2-overexpressing cells (Fig. 10B and C). These findings strongly suggested that overexpression of DUSP2 aggravated APAP-induced mitochondrial apoptosis and suppressed the anti-apoptosis effect of **10**. Furthermore, a drug affinity responsive target stability (DARTS) technology was conducted. The results revealed that proteolysis of DUSP2 was significantly decreased in the presence of **10** (Fig. 10D and E). The thermal stability of DUSP2 was also examined by cellular thermal shift assay (CETSA) approach, which suggested that **10** could stabilize DUSP2 at higher temperatures (Fig. 10F and G). Taken together, these findings suggest a potential interaction between DUSP2 and **10**. Mechanistically, **10** alleviated mitochondria-mediated apoptosis by suppressing the DUSP2-mediated PI3K/Akt/JNK pathway, thus ameliorating APAP-induced liver injury.

3. Discussion

Twelve novel spirocyclic heterodimeric alkaloids **1**−**12** with 5/6/6/6/5 and 6/5/6/6/5 pentacyclic skeletons were isolated from *S. flavescens*. Structurally, these compounds represent unprecedented heterodimeric scaffolds consisting of C_{15} matrine-type alkaloid and non-alkaloid C_9 units. Characteristically, the inert six-membered ring A or B of the C_{15} unit was rearranged into a five-membered ring, followed by the establishment of an unprecedented azaspiro[4.4] ring through the fusion with the C_9 unit. These findings provide reasonable patterns for diverse derivative syntheses of inactive rings A or B of matrine-type alkaloids. In addition, the additive patterns of the C_9 unit with several matrine-type alkaloids allowed us to speculate that they were generated through the similar biosynthetic pathways. Taking compounds **1** and **2** as examples, the synthesis of these alkaloids begins with the decarboxylation of L-lysine by lysinedecarboxylase (LDC) to form the intermediate cadaverine[29]. Cadaverine undergoes several steps to generate sophocarpine[30], which could be oxidized and then hydrolyzed to yield intermediates **A1** and **A2**[3]. Then, **A2** could be cyclized to form **A3**. **A3** could subsequently be coupled with a 2-hydroxy-3-(4-hydroxyphenyl)allylium unit produced by piscidic acid (a highly abundant constituent in *S. flavescens*), to generate intermediate **A4** through a possible [3 + 2] cycloaddition reaction. Finally, **A4** could be dehydrated to yield **1** and **2** (Scheme 1).

The liver is one of the vital organs responsible for the digestion and storage of nutrients, disposal of harmful substances, synthesis of proteins, and secretion of bile[31]; however, it is vulnerable to hepatitis virus and drug toxicity. Drug-induced liver injury is a prevalent form of liver damage attributed to drug overdose, resulting in liver failure and even liver cancer[1]. As a commonly prescribed antipyretic and analgesic agent, APAP was found to cause acute liver injury and hepatotoxicity with overdose[32]. Previous research has revealed that excessive APAP is catalyzed into *N*-acetyl-*p*-benzoquinoneimine (NAPQI) by cytochrome P450 (CYP) and that excess NAPQI depletes GSH, leading to oxidative stress and mitochondrial dysfunction, followed by the acute liver injury[33,34]. NAC is the only FDA-approved treatment for APAP hepatotoxicity but has a short effective drug duration[35]. Matrine is a representative compound of *S. flavescens* and was found to exhibit hepatoprotective activity in liver injury and liver fibrosis[36]. Our results showed that **10**, a spirocyclic heterodimeric alkaloid, increased the viability of APAP-induced HepG2 cells *in vitro* better than that of NAC and matrine did (Fig. 6B and C). Further evaluation of hepatoprotective activity *in vivo* revealed that **10** significantly decreased the serum ALT, AST, and LDH levels, reversed the depletion of hepatic GSH, and improved hepatocellular necrosis and hemorrhaging of liver tissues. These findings

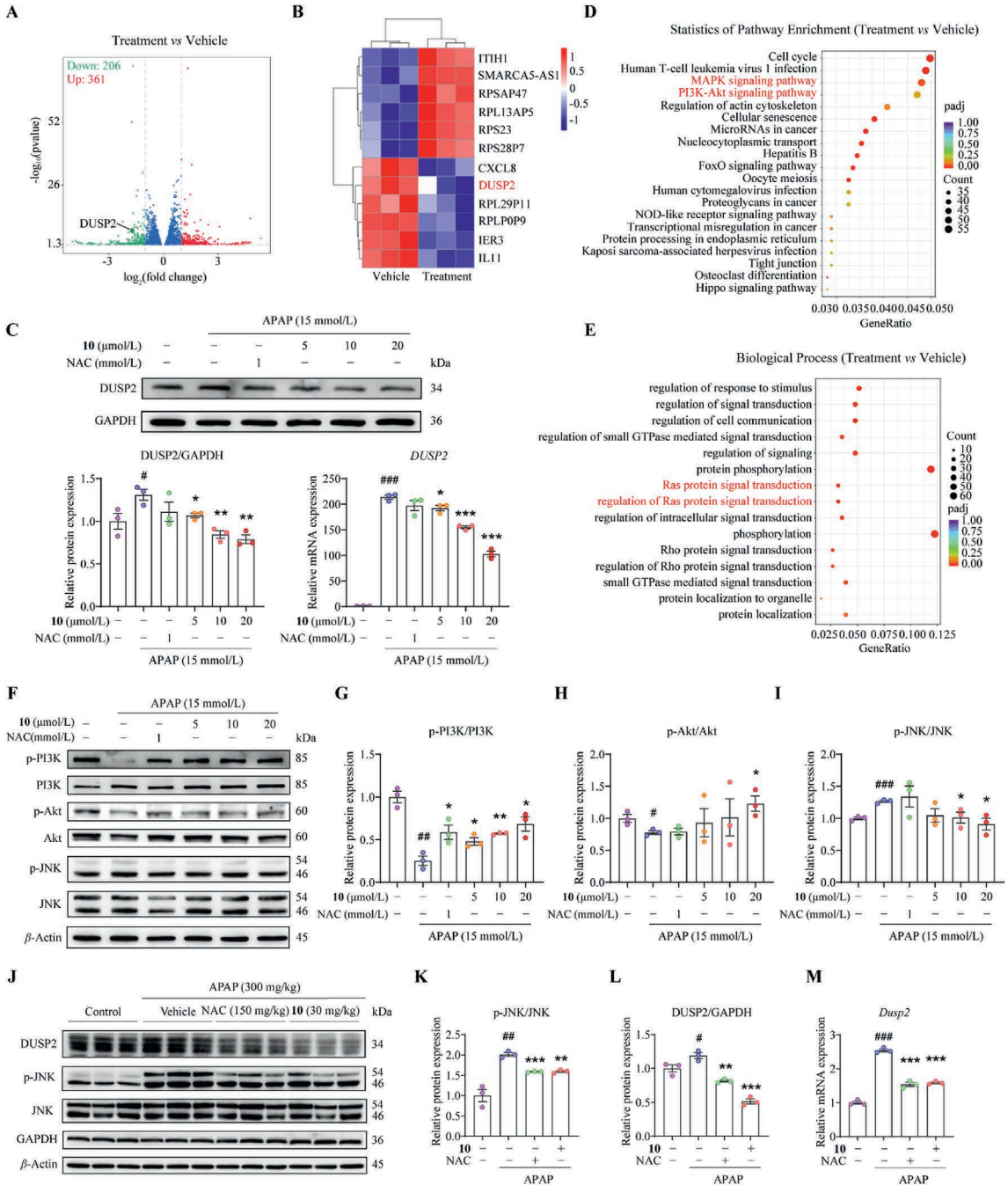

Figure 9 Compound **10** exhibits hepatoprotective activity by inhibiting PI3K/Akt/JNK pathway. (A) Using RNA-seq and gene set enrichment analysis, a volcano plot of the treated group (10 μmol/L) and APAP group displayed DEGs in APAP-induced HepG2 cells. The upregulated genes are shown in red, the downregulated genes are shown in green, and genes with no significant change are shown in blue, $n = 3$ per group. (B) Heatmap revealing the expression of DEGs in the treated group (10 μmol/L) and APAP group. (C) Western blots and real time quantitative PCR results for DUSP2 in APAP-induced HepG2 cells. GAPDH served as the loading control. (D, E) KEGG pathway and Gene Ontology biological process bubble diagrams of DEGs altered in the **10**-treated HepG2 cells, compared with the APAP-treated HepG2 cells, showing the enrichment of biological processes and pathways. The abscissa is the gene ratio, and the ordinates indicate the GO enrichment biological process and the KEGG enrichment pathway, respectively. Bubble size represents the number of DEGs, and bubble color represents the enrichment significance. (F−I) Western blots and quantification results of p-PI3K/PI3K, p-Akt/Akt, and p-JNK/JNK in HepG2 cells. β-Actin served as the loading control. (J−L) Western blots and quantification results of DUSP2 and *p*-JNK/JNK in liver tissues. β-Actin or GAPDH served as the loading control. (M) Real time quantitative PCR results for *Dusp2* in liver tissues. Data are expressed as mean ± SEM of three independent experiments, $^{\#}P < 0.05$, $^{\#\#}P < 0.01$, and $^{\#\#\#}P < 0.001$ compared with the control group, $^{*}P < 0.05$, $^{**}P < 0.01$, and $^{***}P < 0.001$ compared with the APAP group.

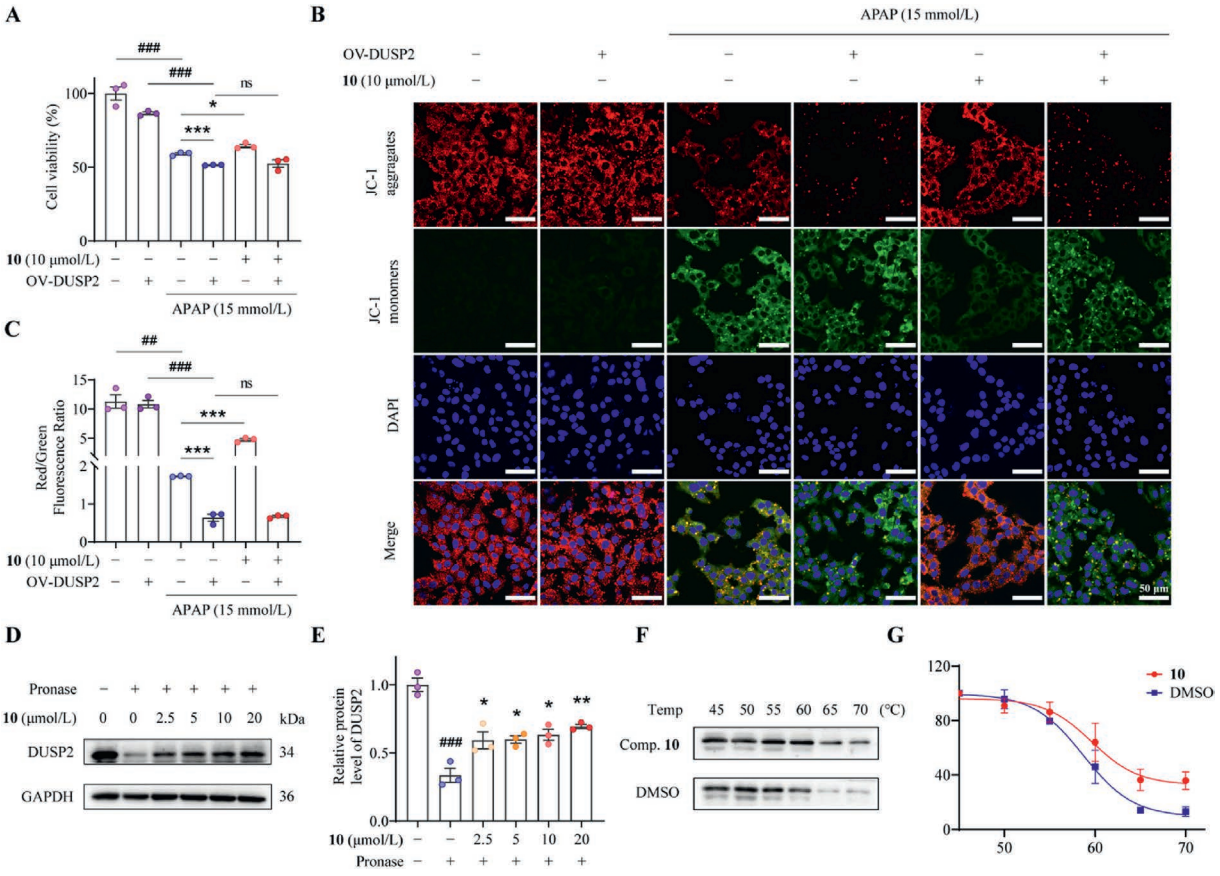

Figure 10 Compound **10** exhibits hepatoprotective activity through targeting DUSP2. (A) Cell viability of **10** on APAP-induced overexpression DUSP2 cells. (B) Representative images of JC-1-stained HepG2 cells ($n = 3$, original magnification of 60 ×) in the control, APAP, and treated overexpression DUSP2 cells. Scale bar, 50 μm. (C) Quantification of the red/green fluorescence ratio determined *via* image J. (D,E) DARTS analysis between **10** and DUSP2. Protein levels at concentrations of 2.5, 5, 10, and 20 μmol/L in the treated groups were examined. Data are expressed as mean ± SEM of three independent experiments, $^{\#\#}P < 0.01$, $^{\#\#\#}P < 0.001$, and not significant (ns), $^{*}P < 0.05$, $^{**}P < 0.01$, and $^{***}P < 0.001$. (F,G) CETSA analysis between **10** and DUSP2. Protein levels were examined at different temperatures in the treated groups (10 μmol/L).

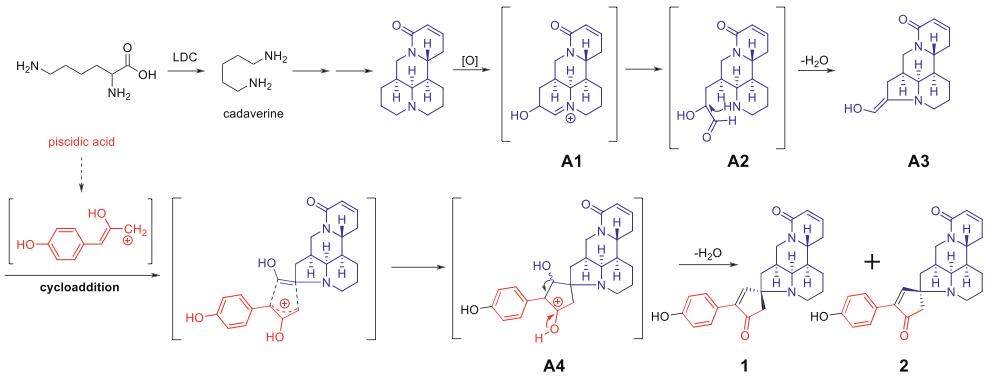

Scheme 1 Plausible biosynthetic pathway of spirocyclic heterodimeric alkaloids.

demonstrated that **10** could serve as a therapeutic candidate for liver injury.

Apoptosis is a noninflammatory biological process since phagocytic cells can rapidly eliminate apoptotic cells. Hepatocyte apoptosis frequently results in liver injury, liver fibrosis, and inflammation[37,38]. Mitochondria are the primary intracellular organelles targeted by APAP. Mitochondrial dysfunction occurs during the early stages of APAP-induced liver injury[39]. In particular, mitochondrial apoptosis is involved in the progression of liver injury[40,41]. To investigate the effect of **10** on APAP-induced apoptosis, TUNEL and Annexin-V FITC/PI staining were employed to determine the degree of apoptosis, and JC-1

staining was used to determine the mitochondrial membrane potential. Our results showed that **10** significantly inhibited cell apoptosis in a dose-dependent manner *in vitro*, and diminished hepatocyte apoptosis *in vivo*. Furthermore, the downregulation of the proapoptotic proteins Bax, cleaved caspase-3, and cleaved caspase-9 and the upregulation of antiapoptotic protein Bcl-2 in the treated groups suggested that **10** exhibited hepatoprotective effect by restricting mitochondrial apoptosis.

Dual-specificity phosphatases (DUSPs) are responsible for regulating mitogen-activated protein kinase (MAPK) signaling pathways. As a member of the DUSP family, DUSP2 is predominantly expressed in liver tissues with high T-cell content. DUSP2 serves as a proapoptotic protein and plays an important role in cell apoptosis[42,43]. Previous investigations have shown that DUSP2 is involved in the mechanisms of cardioprotective, nephroprotection, and neuroprotection activities[44-46] but has not been reported in acute liver injury. Here, through transcriptomic analysis, we found that the expression of *DUSP2* was upregulated in APAP-induced cells compared with the control cells and downregulated in treated cells. Real time quantitative PCR and Western blotting were further performed to verify the expression of DUSP2 *in vitro* and *in vivo*. Unexpectedly, APAP treatment showed higher mRNA expression of DUSP2 in HepG2 cells than in mice. This difference may be due to the inhibitory effect of systemic regulation on transcription *in vivo*[47]. Moreover, overexpression of DUSP2 aggravated APAP-induced mitochondrial apoptosis and **10** failed to reverse the apoptosis. Notably, DARTS and CETSA assays revealed that DUSP2 became protease-resistant and thermostable in the presence of **10**. These results indicated that **10** exhibits a potential interaction with DUSP2 and inhibits mitochondrial apoptosis. This represents the first discovery of the involvement of DUSP2 in the hepatoprotective mechanism. Thus, the DUSP2-mediated MAPK signaling pathway was further identified as a major mechanism by which **10** affects APAP-induced livery injury.

MAPK activation cascades mediate various physiological processes, including cell proliferation, differentiation, stress responses, inflammation, and apoptosis[42,48]. MAPK signaling involves four pathways and the JNK signaling pathway is mainly involved in apoptosis[28,49]. Given that **10** inhibits mitochondrial apoptosis and is involved in the regulation of the MAPK signaling pathway, we focused on the JNK signaling pathway and confirmed that **10** decreased the protein expression of p-JNK/JNK in HepG2 cells and liver tissues. Moreover, the PI3K/Akt-mediated apoptosis signaling pathway has been proposed to alleviate APAP-induced liver injury[50-52]. RNA-seq revealed that the PI3K-Akt signaling pathway, which is upstream of the JNK signaling pathway, was enriched in the KEGG analysis. The protein expression of p-PI3K/PI3K and p-Akt/Akt demonstrated that **10** activated the PI3K−Akt signaling pathway. Combined with the protein and mRNA expression of DUSP2, **10** exerted hepatoprotective activity by inhibiting the DUSP2-mediated PI3K/Akt/JNK pathway, thereby ameliorating APAP-induced mitochondrial apoptosis.

4. Conclusions

In summary, a targeted strategy integrating BBMN, NAP, UV, and MS was employed to guide the isolation of distinctive matrine-based alkaloid dimers. Twelve novel spirocyclic heterodimeric alkaloids (**1**−**12**) possessing 5/6/6/6/5 and 6/5/6/6/5 pentacyclic skeletons were isolated from *S. flavescens*, representing the first examples of azaspiro[4.4] alkaloids formed with unprecedented C_{15} and C_9 units. The structures of these compounds were unambiguously elucidated *via* extensive spectroscopic methods, quantum chemical calculations, and single-crystal X-ray diffraction. Additionally, the ^{1}H and ^{13}C NMR data of C-9′ can be used as diagnostic signals to determine the absolute configuration of the spiro carbon. A hypothetical biosynthetic pathway for these compounds was proposed. Moreover, the hepatoprotective effects of compounds **1**−**12** were evaluated *in vitro*. **10** significantly ameliorated hepatic centrilobular necrosis and bleeding, decreased the serum ALT, AST, and LDH levels, and reversed the rapid consumption of GSH, resulting in significant hepatoprotective activity *in vivo*. Flow cytometry, immunofluorescence assays, and Western blots indicated that **10** could inhibit mitochondrial apoptosis. Immunoblotting, DARTS, and CETSA verified that **10** exhibits a potential interaction with DUSP2 and inhibits its expression, suppressing DUSP2-mediated mitochondrial apoptosis *via* PI3K/Akt/JNK pathway. Our findings indicate that **10** might be a promising candidate for the treatment of acute liver injury and is worthy of further exploration and development.

5. Experimental

5.1. General experimental procedures

Detailed experimental procedures are provided in Supporting Information.

5.2. Plant material

The roots of *S. flavescens* were purchased from Beijing PushengLin Pharmaceutical Company. The plant material was authenticated by Prof. L. Ma. A voucher specimen (ID-5-2438) was deposited at the Institute of Materia Medica, Chinese Academy of Medical Sciences, Beijing, China.

5.3. Extraction and isolation

The air-dried powdered roots of *S. flavescens* (100 kg) were percolated with 1% aqueous AcOH (1 × 24 h) and then decocted with H_2O (2 × 1 h). The filtrate was concentrated to obtain a crude extract (6.5 kg), which was subjected to an HP-20 macroporous resin column eluted with a gradient of EtOH/H_2O to give fractions A−F. Fraction E (223 g) was separated by a silica gel column (200−300 mesh) eluted with a gradient of CH_2Cl_2/MeOH (100:1−1:100) to yield seventeen subfractions (E1−E17). Fraction E6 (1.4 g) was chromatographed on an ODS gel column eluted with H_2O/MeOH (90:10 to 30:70) to afford five subfractions (E6A−E6E). Subfraction E6C (178 mg) was separated by semi-preparative HPLC on a YMC column (MeCN/H_2O, 30:70, *v*/*v*), followed by chiral separation on a Chiralpak AD-RH column (MeCN/H_2O, 45:55, *v*/*v*) to provide **3** (39.0 mg) and **4** (11.7 mg). Fraction E7 (6 g) was purified on a RP-C18 column employing mobile phase H_2O/MeOH (90:10 to 30:70), generating ten subfractions (E7A−E7J). Subfraction E7H (64 mg) was separated by semi-preparative HPLC (MeCN/H_2O, 35:65, *v*/*v*) to yield **1** (6.7 mg) and **2** (15.6 mg). Fraction E8 (4.4 g) was fractioned by an ODS column using H_2O/MeOH as mobile phase (from 80:20 to 20:80) to yield five subfractions (E8A−E8E). Subfraction E8D (132 mg) was purified by semi-preparative

HPLC (MeCN/H_2O, 35:65, *v*/*v*) to obtain **12** (2.1 mg). Fraction E9 (1.6 g) was chromatographed over a RP-C18 column (H_2O/MeOH, 90:10 to 20:80) to afford eight subfractions (E9A−E9H). Subfraction E9F (216 mg) was purified by semi-preparative HPLC (MeOH/H_2O, 55:45, *v*/*v*), followed by a chiral resolution (MeCN/H_2O, 50:50, *v*/*v*) to provide **7** (16.1 mg) and **8** (72.4 mg). Subfraction E9G (133 mg) was separated by semi-preparative HPLC on a YMC column (MeCN/H_2O, 35:65, *v*/*v*) and a Waters column (0.02% $NH_3 \cdot H_2O$, MeOH/MeCN/H_2O, 35:5:60, *v*/*v*/*v*) to obtain **5** (43.7 mg) and **6** (4.4 mg). Fraction E11 (4.4 g) was fractioned by an ODS gel column employing H_2O/MeOH as mobile phase (80:20 to 20:80) to yield seven fractions (E11A−E11G). Fraction E11E (39 mg) was separated by semi-preparative HPLC (MeCN/H_2O, 35:65, *v*/*v*) to produce **11** (8.0 mg). Fraction E12 (9.5 g) was chromatographed on ODS (H_2O/MeOH, 90:10 to 20:80) to afford five subfractions (E12A−E12E). Subfraction E12B (160 mg) was purified by semi-preparative HPLC (MeCN/H_2O, 25:75, *v*/*v*) to give **10** (33.3 mg). Subfraction E12D (54 mg) was separated by semi-preparative HPLC (MeOH/H_2O, 50:50, *v*/*v*) to provide **9** (8.5 mg).

*Flavescensine A (**1**)*: yellowish-white amorphous powder; $[\alpha]_D^{20}$ +26.0 (*c* 0.10, MeOH); UV (MeOH) λ_{max} (log ε): 203 (4.36), 239 (4.04), 279 (3.82), 304 (3.68) nm; IR ν_{max}: 2932, 1702, 1660, 1595, 1512, 1436, 1326, 1270, 1242, 1138, 837 cm $^{-1}$; ^{1}H and ^{13}C NMR data, see Table S1; HRESIMS *m*/*z* 391.2010 $[M + H]^+$ (calcd for $C_{24}H_{27}O_3N_2$, 391.2016); ECD (*c* 0.25 mg/mL, MeOH) λ_{max} ($\Delta\varepsilon$): 211 (−7.05), 236 (+0.92), 261 (−5.96), 305 (+10.26), 348 (−3.58) nm (Supporting Information Fig. S18−S27).

*Flavescensine B (**2**)*: yellowish-white amorphous powder; $[\alpha]_D^{20}$ −8.0 (*c* 0.10, MeOH); UV (MeOH) λ_{max} (log ε): 203 (4.45), 236 (4.17), 280 (3.94), 303 (3.80) nm; IR ν_{max}: 2936, 1698, 1657, 1587, 1512, 1484, 1378, 1324, 1272, 1142, 840 cm $^{-1}$; ^{1}H and ^{13}C NMR data, see Table S1; HRESIMS *m*/*z* 391.2015 $[M + H]^+$ (calcd for $C_{24}H_{27}O_3N_2$, 391.2016); ECD (*c* 0.2 mg/mL, MeOH) λ_{max} ($\Delta\varepsilon$): 213 (+3.17), 283 (−4.26), 339 (+3.72) nm (Supporting Information Fig. S28−S37).

*Flavescensine C (**3**)*: yellowish-white amorphous powder; $[\alpha]_D^{20}$ −77.0 (*c* 0.10, MeOH); UV (MeOH) λ_{max} (log ε): 203 (4.27), 237 (3.92), 280 (3.70), 303 (3.56) nm; IR ν_{max}: 2932, 1702, 1661, 1636, 1597, 1512, 1429, 1367, 1272, 1090, 835 cm $^{-1}$; ^{1}H and ^{13}C NMR data, see Table S3; HRESIMS *m*/*z* 391.2011 $[M + H]^+$ (calcd for $C_{24}H_{27}O_3N_2$, 391.2016); ECD (*c* 0.2 mg/mL, MeOH) λ_{max} ($\Delta\varepsilon$): 220 (+2.83), 244 (−4.02), 297 (+1.36), 339 (−1.93) nm (Supporting Information Fig. S38−S47).

*Flavescensine D (**4**)*: yellowish-white amorphous powder; $[\alpha]_D^{20}$ −135.0 (*c* 0.10, MeOH); UV (MeOH) λ_{max} (log ε): 204 (4.45), 239 (4.13), 279 (3.90), 304 (3.77) nm; IR ν_{max}: 2929, 1700, 1662, 1597, 1512, 1435, 1385, 1272, 1137, 838 cm $^{-1}$; ^{1}H and ^{13}C NMR data, see Table S3; HRESIMS *m*/*z* 391.2010 $[M + H]^+$ (calcd for $C_{24}H_{27}O_3N_2$, 391.2016); ECD (*c* 0.2 mg/mL, MeOH) λ_{max} ($\Delta\varepsilon$): 204 (+9.52), 300 (−7.27), 347 (+2.16) nm (Supporting Information Fig. S48−S57).

*Flavescensine E (**5**)*: yellowish-white amorphous powder; $[\alpha]_D^{20}$ +66.0 (*c* 0.10, MeOH); UV (MeOH) λ_{max} (log ε): 203 (4.28), 281 (3.66), 307 (3.57) nm; IR ν_{max}: 2935, 1703, 1611, 1512, 1441, 1335, 1273, 1244, 1139, 838 cm $^{-1}$; ^{1}H and ^{13}C NMR data, see Table S1; HRESIMS *m*/*z* 393.2163 $[M + H]^+$ (calcd for $C_{24}H_{29}O_3N_2$, 393.2173); ECD (*c* 0.167 mg/mL, MeOH) λ_{max} ($\Delta\varepsilon$): 221 (−6.13), 243 (+1.97), 262 (−0.81), 303 (+8.17), 347 (−2.71) nm (Supporting Information Fig. S58−S67).

*Flavescensine F (**6**)*: yellowish-white amorphous powder; $[\alpha]_D^{20}$ −7.0 (*c* 0.10, MeOH); UV (MeOH) λ_{max} (log ε): 203 (4.26), 281 (3.61), 305 (3.50) nm; IR ν_{max}: 2924, 2852, 1703, 1608, 1513, 1438, 1362, 1272, 837 cm $^{-1}$; ^{1}H and ^{13}C NMR data, see Table S2; HRESIMS *m*/*z* 393.2163 $[M + H]^+$ (calcd for $C_{24}H_{29}O_3N_2$, 393.2173); ECD (*c* 0.5 mg/mL, MeOH) λ_{max} ($\Delta\varepsilon$): 234 (−0.92), 287 (−1.13), 341 (+0.95) nm (Supporting Information Fig. S68−S77).

*Flavescensine G (**7**)*: yellowish-white amorphous powder; $[\alpha]_D^{20}$ −28.0 (*c* 0.10, MeOH); UV (MeOH) λ_{max} (log ε): 203 (4.24), 280 (3.57), 305 (3.46) nm; IR ν_{max}: 2932, 1702, 1613, 1513, 1444, 1273, 1027, 838 cm $^{-1}$; ^{1}H and ^{13}C NMR data, see Table S3; HRESIMS *m*/*z* 393.2162 $[M + H]^+$ (calcd for $C_{24}H_{29}O_3N_2$, 393.2173); ECD (*c* 0.25 mg/mL, MeOH) λ_{max} ($\Delta\varepsilon$): 215 (+2.94), 244 (−0.25), 284 (+2.28), 338 (−2.67) nm (Supporting Information Fig. S78−S87).

*Flavescensine H (**8**)*: yellowish-white amorphous powder; $[\alpha]_D^{20}$ −42.0 (*c* 0.10, MeOH); UV (MeOH) λ_{max} (log ε): 203 (4.25), 282 (3.58), 305 (3.51) nm; IR ν_{max}: 2934, 1704, 1609, 1512, 1444, 1368, 1265, 1139, 837 cm $^{-1}$; ^{1}H and ^{13}C NMR data, see Supporting Information Table S4; HRESIMS *m*/*z* 393.2162 $[M + H]^+$ (calcd for $C_{24}H_{29}O_3N_2$, 393.2173); ECD (*c* 0.25 mg/mL, MeOH) λ_{max} ($\Delta\varepsilon$): 207 (+12.50), 241 (−1.27), 260 (+0.79), 302 (−8.58), 348 (+2.81) nm (Supporting Information Fig. S88−S97).

*Flavescensine I (**9**)*: yellowish-white amorphous powder; $[\alpha]_D^{20}$ −44.0 (*c* 0.10, MeOH); UV (MeOH) λ_{max} (log ε): 203 (4.38), 221 (4.14), 282 (3.80), 304 (3.73) nm; IR ν_{max}: 2937, 1706, 1608, 1513, 1456, 1414, 1327, 1203, 1152, 839 cm $^{-1}$; ^{1}H and ^{13}C NMR data, see Table S4; HRESIMS *m*/*z* 393.2177 $[M + H]^+$ (calcd for $C_{24}H_{29}O_3N_2$, 393.2173); ECD (*c* 0.2 mg/mL, MeOH) λ_{max} ($\Delta\varepsilon$): 217 (−1.65), 283 (+2.92), 339 (−2.51) nm (Supporting Information Fig. S98−S107).

*Flavescensine J (**10**)*: yellowish-white amorphous powder; $[\alpha]_D^{20}$ −123.0 (*c* 0.10, MeOH); UV (MeOH) λ_{max} (log ε): 203 (4.39), 237 (4.08), 282 (3.72), 308 (3.63) nm; IR ν_{max}: 2935, 1704, 1609, 1512, 1463, 1415, 1327, 1274, 1235, 1144, 838 cm $^{-1}$; ^{1}H and ^{13}C NMR data, see Table S4; HRESIMS *m*/*z* 393.2167 $[M + H]^+$ (calcd for $C_{24}H_{29}O_3N_2$, 393.2173); ECD (*c* 0.25 mg/mL, MeOH) λ_{max} ($\Delta\varepsilon$): 213 (+11.13), 239 (−1.01), 258 (+0.36), 301 (−9.79), 348 (+2.65) nm (Supporting Information Fig. S108−S117).

*Flavescensine K (**11**)*: yellowish-white amorphous powder; $[\alpha]_D^{20}$ +166.0 (*c* 0.10, MeOH); UV (MeOH) λ_{max} (log ε): 202 (4.42), 228 (4.27), 308 (4.14) nm; IR ν_{max}: 2935, 1706, 1654, 1553, 1512, 1466, 1274, 1144, 839 cm $^{-1}$; ^{1}H and ^{13}C NMR data, see Table S2; HRESIMS *m*/*z* 389.1857 $[M + H]^+$ (calcd for $C_{24}H_{25}O_3N_2$, 389.1860); ECD (*c* 0.25 mg/mL, MeOH) λ_{max} ($\Delta\varepsilon$): 225 (−5.72), 269 (−1.93), 306 (+5.71) nm (Supporting Information Fig. S118−S127).

Flavescensine L *(**12**)*: yellow amorphous powder; $[\alpha]_D^{20}$ −136.0 (*c* 0.10, MeOH); UV (MeOH) λ_{max} (log ε): 202 (4.30), 236 (4.28), 279 (3.81), 304 (3.72) nm; IR ν_{max}: 2930, 1704, 1622, 1513, 1435, 1404, 1269, 1177, 839 cm $^{-1}$; ^{1}H and ^{13}C NMR data, see Table S2; HRESIMS *m*/*z* 391.2012 $[M + H]^+$ (calcd for $C_{24}H_{27}O_3N_2$, 391.2016); ECD (*c* 0.1 mg/mL, MeOH) λ_{max} ($\Delta\varepsilon$): 247 (−16.17), 335 (+0.91) nm (Supporting Information Fig. S128−S137).

5.4. X-ray crystal structure analysis

Single-crystal X-ray diffraction data of compounds **1**−**12** were obtained on a 'Bruker APEX-II CCD' diffractometer using Cu Kα radiation. Crystallographic data for these compounds have been deposited at the Cambridge Crystallographic Data Centre with

codes of 2416436-2416447. Supporting Information presented the detailed crystal data of compounds **1**−**12**.

5.5. Quantum chemical calculations

To determine the relative configurations, several possible isomers of **1**, **3**, **4**, and **7** were calculated at the mPW1PW91/6-31+g(d,p) and B3LYP/6-31+g(d,p) levels in pyridine using Gaussian 16. The calculated NMR was the sum of conformation data multiplied by their respective Boltzmann distribution. Regression and custom DP4+ probability methods were further performed to compare the calculated values with the experimental NMR data (Supporting Information Tables S5−S20 and Figs. S5−S16). Based on the relative configurations elucidated by NMR calculations, ECD curves of enantiomers of **1** were calculated at the CAM-B3LYP/6-31+g(d,p) level in methanol (Supporting Information Fig. S17).

5.6. Cell viability assay

HepG2 cells were cultured in Dulbecco's modified eagle media (DMEM, HyClone, SH30022.01) with 10% fetal bovine serum and 100 U/mL penicillin-streptomycin in 5% CO_2, 37 °C. Cell viability was measured by CCK-8 assay. HepG2 cells were seeded in 96-well culture plates with 5000 cells per well and incubated for 24 h. Then, HepG2 cells were cotreated with APAP (15 mmol/L) and/or the test compounds (10 μmol/L), and NAC (1 mmol/L) was used as the positive control. After 24 h incubation, 10 μL CCK-8 was added per well and incubated for another 2 h, and the absorbance values were finally detected by a microplate reader at 450 nm.

5.7. Cell apoptosis analysis

HepG2 cells were inoculated in 6-well plates at a density of 1×10^6 cells per well and cultured for 24 h. To investigate the effect of **10** on APAP-induced apoptosis, HepG2 cells were cotreated with APAP (15 mmol/L) and/or **10** (5, 10, and 20 μmol/L), and NAC (1 mmol/L) was used as the positive control. After 24 h incubation, cells were digested with trypsin and washed with pre-cooled PBS three times. Then, 195 μL Annexin V-FITC binding buffer, 5 μL FITC, and 10 μL PI (Beyotime, C1062) were added and cells were incubated for 15 min at room temperature in a dark environment. The apoptotic rate was examined by flow cytometry.

5.8. Cell cycle analysis

After incubation with **10** and APAP, HepG2 cells were collected and fixed by pre-cooled 70% ethanol overnight. Then, cells were added 0.5 mL staining buffer, 25 μL PI and 10 μL RNase A (Beyotime, C1052), and incubated for 30 min at 37 °C in a dark environment. The cell cycle results were detected by flow cytometry.

5.9. JC-1 staining

After incubation with **10** and APAP, HepG2 cells were added 0.5 mL culture medium and 0.5 mL JC-1 staining solution (Solarbio, M8650), and incubated for 20 min at 37 °C in a dark environment. Then, cells were washed with JC-1 buffer solution two times. The results were detected by Confocal Laser Scanning Microscopy and analyzed by image J software (Media Cybernetics, Bethesda, MD, USA).

5.10. MPTP staining

After incubation with **10** and APAP, HepG2 cells were added 1 mL fluorescence quenching solution (Beyotime, C2009S), and incubated for 30 min at 37 °C in a dark environment. Then, fluorescence quenching solution were replaced by DMEM, and incubated for 30 min at 37 °C in a dark environment. Finally, cells were washed with PBS two times. The results were detected by Confocal Laser Scanning Microscopy and analyzed by image J software (Media Cybernetics, Bethesda, MD, USA).

5.11. RNA-seq analysis

HepG2 cells were inoculated in T75 at a density of 1×10^7 cells and cultured for 24 h. Then, HepG2 cells were treated with APAP (15 mmol/L) or cotreated with APAP (15 mmol/L) and **10** (10 μmol/L) for 24 h, and total RNA was extracted from APAP-treated HepG2 cells using TRIzol (ThermoFisher, 15596026CN). Three samples obtained from the control, vehicle, and treated group were sent to Novogene (Beijing) for the extraction, purification, and enrichment of total RNA, sequencing by Illumina PE150, and creating the specific RNA library. The results of DEGs and analysis of GO enrichment biological process and the KEGG enrichment pathway were performed.

5.12. Real time quantitative PCR

Total RNA was extracted from HepG2 cells and liver tissues using TRIzol (ThermoFisher, 15596026CN) and the cDNAs were synthesized from the corresponding RNA with PrimeScript™ RT reagent Kit (Takara, RR037A). Real time quantitative PCR was conducted using Taq Pro Universal SYBR qPCR Master Mix (Vazyme, Q712). Combined with the expression of reference gene β-actin, the results of target gene were quantified by $2^{-\Delta\Delta Ct}$ method, which expressed as a ratio compared to the control group. Primer sequences used in the Real time quantitative PCR experiment are shown in Supporting Information Table S21.

5.13. Drug affinity responsive target stability (DARTS) experiment

Lysates of HepG2 cells were treated with **10** (2.5, 5, 10, and 20 μmol/L) for 6 h. Then, the protein solutions were incubated with 20 μg/ml pronase at 37 °C for 30 min. The reactions were terminated by adding loading buffer and boiled for 10 min at 100 °C. The expression levels of DUSP2 were analyzed by Western blots.

5.14. Cellular thermal shift assay (CETSA)

Lysates of HepG2 cells were treated with **10** (10 μmol/L) or 0.1% DMSO for 6 h. Then, solutions were heated at different temperatures (from 45 to 70 °C) for 3 min and cooled on ice quickly. The solutions were subsequently added with loading buffer and Western blots were performed to examine the levels of DUSP2.

5.15. Western blotting

Proteins were extracted from APAP-treated HepG2 cells or liver tissues using RIPA buffer (Beyotime, P0013C) with protease and phosphatase inhibitors, which was followed by quantification of total protein content determined by the BCA method. The lysates were added with 5 × loading buffer (Beyotime, P0015L) and boiled for 10 min at 100 °C. After that, proteins were subjected to SDS-PAGE gels and transferred to PVDF membranes, followed by blocking with 5% (*w*/*v*) skim milk for 2 h at room temperature. Membranes were further incubated with primary antibodies at 4 °C overnight. The primary antibodies included Phospho-PI3K (4228; 1:1000), PI3K (4257; 1:1000), Phospho-Akt (4060; 1:1000), Akt (4691; 1:1000), Caspase-9 (9508; 1:1000), Caspase-3 (9662; 1:1000), Cleaved-caspase-3 (9664; 1:1000), Bax (2772; 1:1000), Bcl-2 (3498; 1:1000), Phospho-JNK (4668; 1:1000), JNK (9252; 1:1000), which were obtained from Cell Signaling Technology. The primary antibody Phospho-PI3K (ab138364; 1:1000) was obtained from Abcam. The primary antibody β-Actin (bsm-33036M; 1:1000) was obtained from Bioss Antibodies. The primary antibody DUSP2 (A16366; 1:1000) was obtained from ABclonal. The primary antibody GAPDH (60004-1-Ig; 1:10,000) was obtained from Proteintech. On the second day, membranes were washed with TBST and incubated with HRP-conjugated secondary antibodies for 1.5 h at room temperature. The secondary antibodies included Goat anti-mouse IgG coupled with HRP (ZB-2305, 1:10,000) and Goat anti-rabbit IgG coupled with HRP (ZB-5301, 1:10,000), which were obtained from ZSGB-BIO. Next, membranes were washed with TBST, detected by ECL solution (APPLYGEN, P1050), and quantified by image J software (Media Cybernetics, Bethesda, MD, USA).

5.16. Animal experiments

All animal experiments were approved by the Animal Experimentation Ethics Committee of Chinese Academy of Medical Sciences (ethics number: 00001531), and all procedures were carried out in accordance with the guidelines of the Institutional Animal Care and Use Committees of the Chinese Academy of Medical Sciences. 6−8 weeks aged male C57BL/6 mice purchased from SPF (Beijing) Biotechnology Co., Ltd., were randomly divided into four groups ($n = 5$) including control, APAP (300 mg/kg), APAP (300 mg/kg) + NAC (150 mg/kg), and APAP (300 mg/kg) + **10** (30 mg/kg). The mice were given compound **10** or positive control NAC by intragastric administration with two doses at a 12 h interval and were fasted after the first oral gavage. One hour after the last gavage, APAP was administrated by intraperitoneal injection. The liver tissues and plasma were collected at 3 and 6 h after the APAP treatment. Compound **10** was dissolved in 10% polysorbate 80 (*v*/*v*) and 90% saline (*v*/*v*), NAC was dissolved in saline, and APAP was dissolved in 60 °C warm saline and cooled to 37 °C. Serum was collected to measure ALT, AST, and LDH levels through employing Automatic Analyzer. Liver tissues were prepared to test GSH using commercial GSH kits (Nan Jing Jian Cheng, A006-2-1).

5.17. Statistical analysis

Data are statistically expressed as mean ± SEM. Unpaired t test or Welch's *t* test were analyzed to compare the control group with the vehicle group or compare the vehicle group with the treated group in GraphPad Prism (GraphPad Software, La Jolla, CA, USA). *P* values < 0.05 were regarded as significant difference.

Acknowledgments

This project was supported by the National Natural Science Foundation of China (No. 81973194).

Author contributions

Xin Lian: Writing − Original Draft, Visualization, Methodology, Investigation, Data Curation. Jianshuang Jiang: Validation. Yanan Yang: Validation. Ziming Feng: Validation. Xu Zhang: Validation. Xiang Yuan: Writing − Review & Editing, Conceptualization, Formal analysis, Supervision. Peicheng Zhang: Writing − Review & Editing, Conceptualization, Formal analysis, Project administration, Funding acquisition.

Conflicts of interest

The authors declare no conflict of interest.

Appendix A. Supporting information

Supporting information to this article can be found online at https://doi.org/10.1016/j.apsb.2025.12.019.

References

1. Bernal W, Wendon J. Acute liver failure. *N Engl J Med* 2013;**369**:2525−34.
2. Ying SY, Li PC, Wang JQ, Chen KQ, Zou Y, Dai MY, et al. TRF-Gln-CTG-026 ameliorates liver injury by alleviating global protein synthesis. *Signal Transduct Target Ther* 2023;**8**:144.
3. Zhang YB, Zhang XL, Chen NH, Wu ZN, Ye WC, Li YL, et al. Four matrine-based alkaloids with antiviral activities against HBV from the seeds of *Sophora alopecuroides*. *Org Lett* 2017;**19**:424−7.
4. Zhang SY, Li W, Nie H, Liao M, Qiu B, Yang YL, et al. Five new alkaloids from the roots of *Sophora flavescens*. *Chem Biodivers* 2018;**15**:e1700577.
5. Fan CL, Zhang YB, Chen Y, Xie P, Wang GC, Tian HY, et al. Alopecuroides A−E, matrine-type alkaloid dimers from the aerial parts of *Sophora alopecuroides*. *J Nat Prod* 2019;**82**:3227−32.
6. Zhang YB, Zhan LQ, Li GQ, Wang F, Wang Y, Li YL, et al. Dimeric matrine-type alkaloids from the roots of *Sophora flavescens* and their anti-hepatitis B virus activities. *J Org Chem* 2016;**81**:6273−80.
7. Yuan X, Jiang JS, Yang YN, Zhang X, Feng ZM, Zhang PC. Three quinolizidine dimers from the seeds of *Sophora alopecuroides* and their hepatoprotective activities. *Chinese Chem Lett* 2022;**33**:2923−7.
8. Zhang YB, Yang L, Luo D, Chen NH, Wu ZN, Ye WC, et al. Sophalines E−I, five quinolizidine-based alkaloids with antiviral activities against the hepatitis B virus from the seeds of *Sophora alopecuroides*. *Org Lett* 2018;**20**:5942−6.
9. He XR, Fang JC, Huang LH, Wang JH, Huang XQ. *Sophora flavescens* ait.: traditional usage, phytochemistry and pharmacology of an important traditional Chinese medicine. *J Ethnopharmacol* 2015;**172**:10−29.
10. Wang HQ, Xia CB, Chen L, Zhao JJ, Tao WW, Zhang X, et al. Phytochemical information and biological activities of quinolizidine alkaloids in *sophora*: a comprehensive review. *Curr Drug Targets* 2019;**20**:1572−86.
11. Ding PL, Liao ZX, Huang H, Zhou P, Chen DF. (+)-12α-Hydroxysophocarpine, a new quinolizidine alkaloid and related anti-HBV

alkaloids from *Sophora flavescens*. *Bioorg Med Chem Lett* 2006;**16**: 1231−5.
12. Liu XJ, Cao MA, Li WH, Shen CS, Yan SQ, Yuan CS. Alkaloids from *Sophora flavescens* aition. *Fitoterapia* 2010;**81**:524−7.
13. Liu GQ, Dong J, Wang H, Hashi Y, Chen SZ. Characterization of alkaloids in *Sophora flavescens* ait. by high-performance liquid chromatography-electrospray ionization tandem mass spectrometry. *J Pharm Biomed Anal* 2011;**54**:1065−72.
14. Li JC, Zhang ZJ, Liu D, Jiang MY, Li RT, Li HM. Quinolizidine alkaloids from the roots of *Sophora flavescens*. *Nat Prod Res* 2022;**36**: 1781−8.
15. Zhang YB, Luo D, Yang L, Cheng W, He LJ, Kuang GK, et al. Matrine-type alkaloids from the roots of *Sophora flavescens* and their antiviral activities against the hepatitis B virus. *J Nat Prod* 2018;**81**: 2259−65.
16. Wang L, Wu XD, He J, Li GT, Peng LY, Li Y, et al. A new quinolizidine qlkaloid from *Sophora flavescens*. *Chem Nat Compd* 2014;**50**: 876−9.
17. Song JG, Huang RL, Cai JL, Wu ZL, Hu LJ, Sun WY, et al. Targeted isolation of antiviral cinnamoylphloroglucinol-terpene adducts from *cleistocalyx operculatus* by building blocks-based molecular networking approach. *Acta Pharm Sin B* 2024;**14**:4443−60.
18. He QF, Wu ZL, Li L, Sun WY, Wang GY, Jiang RW, et al. Discovery of neuritogenic *securinega* alkaloids from *Flueggea suffruticosa* by a building blocks-based molecular network strategy. *Angew Chem Int Ed Engl* 2021;**60**:19609−13.
19. Lee J, da Silva RR, Jang HS, Kim HW, Kwon YS, Kim JH, et al. *In silico* annotation of discriminative markers of three *zanthoxylum* species using molecular network derived annotation propagation. *Food Chem* 2019;**295**:368−76.
20. Nothias LF, Petras D, Schmid R, Duhrkop K, Rainer J, Sarvepalli A, et al. Feature-based molecular networking in the GNPS analysis environment. *Nat Methods* 2020;**17**:905−8.
21. Cauchie G, N'Nang EO, van der Hooft JJJ, Le Pogam P, Bernadat G, Gallard JF, et al. Phenylpropane as an alternative dearomatizing unit of indoles: discovery of inaequalisines A and B using substructure-informed molecular networking. *Org Lett* 2020;**22**:6077−81.
22. Otogo N, Nang E, Bernadat G, Mouray E, Kumulungui B, Grellier P, et al. Theionbrunonines A and B: dimeric vobasine alkaloids tethered by a thioether bridge from *Mostuea brunonis*. *Org Lett* 2018;**20**:6596−600.
23. Allard PM, Peresse T, Bisson J, Gindro K, Marcourt L, Pham VC, et al. Integration of molecular networking and *in-silico* MS/MS fragmentation for natural products dereplication. *Anal Chem* 2016; **88**:3317−23.
24. Le HTN, Van Roy E, Dendooven E, Peeters L, Theunis M, Foubert K, et al. Alkaloids from *Lepidium meyenii* (Maca), structural revision of macaridine and UPLC−MS/MS feature-based molecular networking. *Phytochemistry* 2021;**190**:112863.
25. Dong YQ, Jia GX, Hu JW, Liu H, Wu TT, Yang SS, et al. Determination of alkaloids and flavonoids in *Sophora flavescens* by UHPLC−Q-TOF/MS. *J Anal Methods Chem* 2021;**2021**:9915027.
26. Bae GH, Lee SK, Kim HS, Lee M, Lee HY, Bae YS. Lysophosphatidic acid protects against acetaminophen-induced acute liver injury. *Exp Mol Med* 2017;**49**:e407.
27. Li XYZ, Lao RY, Lei JW, Chen YT, Zhou Q, Wang T, et al. Natural products for acetaminophen-induced acute liver injury: a review. *Molecules* 2023;**28**:7901.
28. Liao Y, Yang Y, Wang X, Wei M, Guo QL, Zhao L. Oroxyloside ameliorates acetaminophen-induced hepatotoxicity by inhibiting JNK related apoptosis and necroptosis. *J Ethnopharmacol* 2020;**258**:112917.
29. Frick KM, Kamphuis LG, Siddique KH, Singh KB, Foley RC. Quinolizidine alkaloid biosynthesis in lupins and prospects for grain quality improvement. *Front Plant Sci* 2017;**8**:87.
30. Bunsupa S, Yamazaki M, Saito K. Lysine-derived alkaloids: overview and update on biosynthesis and medicinal applications with emphasis on quinolizidine alkaloids. *Mini Rev Med Chem* 2017;**17**:1002−12.
31. Si-Tayeb K, Lemaigre FP, Duncan SA. Organogenesis and development of the liver. *Dev Cell* 2010;**18**:175−89.
32. Yoon E, Babar A, Choudhary M, Kutner M, Pyrsopoulos N. Acetaminophen-induced hepatotoxicity: a comprehensive update. *J Clin Transl Hepatol* 2016;**4**:131−42.
33. Wu YL, Li WX, Zhang JH, Lin JC, You LP, Su J, et al. Shaoyaogancao decoction, a famous Chinese medicine formula, protects against APAP-Induced liver injury by promoting autophagy/mitophagy. *Phytomedicine* 2024;**135**:156053.
34. Liao JQ, Lu QX, Li ZQ, Li JT, Zhao Q, Li J. Acetaminophen-induced liver injury: molecular mechanism and treatments from natural products. *Front Pharmacol* 2023;**14**:1122632.
35. Andrade RJ, Aithal GP, Björnsson ES, Kaplowitz N, Kullak-Ublick GA, Larrey D, et al. EASL clinical practice guidelines: drug-induced liver injury. *J Hepatol* 2019;**70**:1222−61.
36. Zhu JY, Li B, Fang WM, Zhou X, Li DL, Jin JW, et al. Oral matrine alleviates CCl_4-induced liver fibrosis *via* preserved HSP72 from modulated gut microbiota. *Biomed Pharmacother* 2024;**178**:117262.
37. Schwabe RF, Luedde T. Apoptosis and necroptosis in the liver: a matter of life and death. *Nat Rev Gastroenterol Hepatol* 2018;**15**:738−52.
38. Shu YS, He D, Li W, Wang ML, Zhao SY, Liu LL, et al. Hepatoprotective effect of *citrus aurantium* L. against APAP-induced liver injury by regulating liver lipid metabolism and apoptosis. *Int J Biol Sci* 2020;**16**:752−65.
39. Masubuchi Y, Suda C, Horie T. Involvement of mitochondrial permeability transition in acetaminophen-induced liver injury in mice. *J Hepatol* 2005;**42**:110−6.
40. Kim H, Lee JH, Park JW. IDH2 deficiency exacerbates acetaminophen hepatotoxicity in mice *via* mitochondrial dysfunction-induced apoptosis. *Biochim Biophys Acta Mol Basis Dis* 2019;**1865**:2333−41.
41. Yu ZJ, Li Q, Wang Y, Li PF. A potent protective effect of baicalein on liver injury by regulating mitochondria-related apoptosis. *Apoptosis* 2020;**25**:412−25.
42. Chuang HC, Tan TH. MAP4K family kinases and DUSP family phosphatases in T-cell signaling and systemic lupus erythematosus. *Cells* 2019;**8**:1433.
43. Jeffrey KL, Camps M, Rommel C, Mackay CR. Targeting dual-specificity phosphatases: manipulating MAP kinase signalling and immune responses. *Nat Rev Drug Discov* 2007;**6**:391−403.
44. Xu TD, Wu X, Chen QP, Zhu SS, Liu Y, Pan DF, et al. The anti-apoptotic and cardioprotective effects of salvianolic acid A on rat cardiomyocytes following ischemia/reperfusion by DUSP-Mediated regulation of the ERK1/2/JNK pathway. *PLoS One* 2014;**9**:e102292.
45. Xiong JC, Ran L, Zhu YG, Wang YQ, Wang S, Wang YB, et al. DUSP2-mediated inhibition of tubular epithelial cell pyroptosis confers nephroprotection in acute kidney injury. *Theranostics* 2022;**12**: 5069−85.
46. Morente V, Perez-Sen R, Ortega F, Huerta-Cepas J, Delicado EG, Miras-Portugal MT. Neuroprotection elicited by P2Y13 receptors against genotoxic stress by inducing DUSP2 expression and MAPK signaling recovery. *Biochim Biophys Acta* 2014;**1843**:1886−98.
47. Li GP, Sun LF, Xin C, Hao T, Kharel P, Manning AC, et al. A hypoxia-responsive tRNA-derived small RNA confers renal protection through RNA autophagy. *Science* 2025;**389**:eadp5384.
48. Low HB, Zhang YL. Regulatory roles of MAPK phosphatases in cancer. *Immune Netw* 2016;**16**:85−98.
49. Barbier-Torres L, Iruzubieta P, Fernandez-Ramos D, Delgado TC, Taibo D, Guitierrez-de-Juan V, et al. The mitochondrial negative regulator MCJ is a therapeutic target for acetaminophen-induced liver injury. *Nat Commun* 2017;**8**:2068.
50. Ma HC, Ren HZ, Wang J, Yuan XW, Wu XY, Shi XL. Targeting PI3K/Akt/Nrf2 pathway by glabridin alleviates acetaminophen-induced hepatic injury in rats. *Arab J Chem* 2021;**14**:102968.
51. Liu W, Jing ZT, Xue CR, Wu SX, Chen WN, Lin XJ, et al. PI3K/AKT inhibitors aggravate death receptor-mediated hepatocyte apoptosis and liver injury. *Toxicol Appl Pharmacol* 2019;**381**:114729.
52. Yang JY, Zhong YT, Hao WN, Liu XX, Shen Q, Li YF, et al. The PI3K/Akt and NF-κB signaling pathways are involved in the protective effects of *Lithocarpus polystachyus* (sweet tea) on APAP-Induced oxidative stress injury in mice. *RSC Adv* 2020;**10**:18044−53.